remote sensing

MDPI

Article

A Global Climatology of Dust Aerosols Based on Satellite Data: Spatial, Seasonal and Inter-Annual Patterns over the Period 2005–2019

Maria Gavrouzou [1], Nikolaos Hatzianastassiou [1,*], Antonis Gkikas [2], Marios-Bruno Korras-Carraca [1,3] and Nikolaos Mihalopoulos [4,5]

1 Laboratory of Meteorology and Climatology, Department of Physics, University of Ioannina, 45110 Ioannina, Greece; m.gavrouzou@uoi.gr (M.G.); koras@env.aegean.gr (M.-B.K.-C.)
2 Institute for Astronomy, Astrophysics Space Applications and Remote Sensing, National Observatory of Athens, 15236 Athens, Greece; agkikas@noa.gr
3 Department of Environment, University of the Aegean, 81100 Mytilene, Greece
4 Institute for Environmental Research and Sustainable Development (IERSD), National Observatory of Athens, 15236 Athens, Greece; nmihalo@noa.gr
5 Environmental Chemical Processes Laboratory, Department of Chemistry, University of Crete, 70013 Heraklion-Crete, Greece
* Correspondence: nhatzian@uoi.gr; Tel.: +30-26510-08539

Abstract: A satellite-based algorithm is developed and used to determine the presence of dust aerosols on a global scale. The algorithm uses as input aerosol optical properties from the MOderate Resolution Imaging Spectroradiometer (MODIS)-Aqua Collection 6.1 and Ozone Monitoring Instrument (OMI)-Aura version v003 (OMAER-UV) datasets and identifies the existence of dust aerosols in the atmosphere by applying specific thresholds, which ensure the coarse size and the absorptivity of dust aerosols, on the input optical properties. The utilized aerosol optical properties are the multiwavelength aerosol optical depth (AOD), the Aerosol Absorption Index (AI) and the Ångström Exponent (a). The algorithm operates on a daily basis and at $1^\circ \times 1^\circ$ latitude-longitude spatial resolution for the period 2005–2019 and computes the absolute and relative frequency of the occurrence of dust. The monthly and annual mean frequencies are calculated on a pixel level for each year of the study period, enabling the study of the seasonal as well as the inter-annual variation of dust aerosols' occurrence all over the globe. Temporal averaging is also applied to the annual values in order to estimate the 15-year climatological mean values. Apart from temporal, a spatial averaging is also applied for the entire globe as well as for specific regions of interest, namely great global deserts and areas of desert dust export. According to the algorithm results, the highest frequencies of dust occurrence (up to 160 days/year) are primarily observed over the western part of North Africa (Sahara), and over the broader area of Bodélé, and secondarily over the Asian Taklamakan desert (140 days/year). For most of the study regions, the maximum frequencies appear in boreal spring and/or summer and the minimum ones in winter or autumn. A clear seasonality of global dust is revealed, with the lowest frequencies in November–December and the highest ones in June. Finally, an increasing trend of global dust frequency of occurrence from 2005 to 2019, equal to 56.2%, is also found. Such an increasing trend is observed over all study regions except for North Middle East, where a slight decreasing trend (−2.4%) is found.

Keywords: dust; aerosol; satellite; detection; frequency of occurrence; trends; transport

check for updates

Citation: Gavrouzou, M.; Hatzianastassiou, N.; Gkikas, A.; Korras-Carraca, M.-B.; Mihalopoulos, N. A Global Climatology of Dust Aerosols Based on Satellite Data: Spatial, Seasonal and Inter-Annual Patterns over the Period 2005–2019. *Remote Sens.* **2021**, *13*, 359. https://doi.org/10.3390/rs13030359

Received: 31 December 2020
Accepted: 19 January 2021
Published: 21 January 2021

Publisher's Note: MDPI stays neutral with regard to jurisdictional claims in published maps and institutional affiliations.

Copyright: © 2021 by the authors. Licensee MDPI, Basel, Switzerland. This article is an open access article distributed under the terms and conditions of the Creative Commons Attribution (CC BY) license (https://creativecommons.org/licenses/by/4.0/).

1. Introduction

Dust aerosols (DA) is the most abundant aerosol type on Earth [1,2] contributing almost 30% of the total direct aerosol effect on a global basis [3]. The greater part of DA aerosols is injected into the atmosphere from the great deserts, especially from the Sahara [4,5], while a small part comes either from agricultural soils (<10%, remaining in the

lower atmospheric layers, [6]) or from cold high-latitude sources (5%, [7]). DA are injected in the atmosphere under favorable meteorological conditions—cyclonic circulation—above their sources, while they travel over long distances driven by atmospheric circulation. A typical example is the well-known dust export/transport from Northern Africa (Sahara) towards the Tropical Atlantic Ocean, which (during the summer period and especially in July) reaches the eastern coast of N. America and the Caribbean Sea [8]. Large quantities of dust are also transported annually in remote areas such as the Arctic, primarily from Asian deserts [9,10].

DA are very important for various atmospheric processes. They are coarse—with radii varying mainly from 1 to 5 μm [11]—and they absorb mainly solar radiation, inducing direct aerosol effect, while they act as cloud condensation nuclei (CCN) or ice nuclei (IN) [12–18], thus affecting clouds, precipitation and climate (indirect aerosol effect). In general, DA reduce the amount and production rate of precipitation [19] by clouds, thus leading to an increase in their residence time in the atmosphere. In fact, a higher number of CCN leads to more droplets, but with smaller size, and affects the subsequent condensational growth and collision–coalescence [20–23], then delaying the onset of warm rain and modifying the cloud morphology and dynamics [24–26]. Apart from the aerosol effects on warm cloud processes, dust CCNs can also impact the cold cloud processes indirectly by affecting the freezing and riming of liquid drops [27–30], while dust IN may significantly mediate the properties of ice cloud (namely cloud top temperature) through heterogeneous nucleation and lead to crucial impacts on hydrological and energy cycle. In addition, DA also have other effects; for example, they contain minerals that are necessary for several marine biological processes, as well as Fe, which is very important for phytoplankton growth [31–33]. Thus, DA can also affect the global carbon cycle, being deposited and introduced into the oceans.

Due to their high atmospheric loadings, as well as their implication in various atmospheric processes and their effects on weather [34–36], climate, air quality and even human health [37–40], DA are being extensively investigated, especially during the last two decades, on either a regional [41–43] on a global [4,44] scale. Although it has been a considerable effort towards better dust detection and quantification all over the globe, using surface, airborne and satellite-based measurements and model simulations, there is still a high uncertainty about the globally distributed DA. For example, the global dust Aerosol Optical Depth (AOD) or simply Dust Optical Depth (DOD) estimations obtained with climate and chemical transport models are considerably different, by a factor of over 5 [45]. On the other hand, the estimated dust radiative effect, which largely depends on the atmospheric dust load [46], varies from -0.3 to $+0.1$ W/m^2 on a global mean basis [47]. The identification of DA on a global scale is also important for other reasons. For example, the occurrence of dust affects air quality, human health, traffic, the economy and satellite data retrieval, since high AOD values, caused by DA, are often misinterpreted as clouds by satellite retrieval algorithms [10,48]. The DA identification on a multi-year (climatological) basis is also very important for an improved assessment of ongoing climate change and its sources. For example, the presence of dust is one of the most important manifestations of desertification, which is driven by climate change [49,50]. On the other hand, during recent years, there has been evidence for re-activation of dust sources such as Kalahari [51]. For all these reasons, the identification of DA on a global scale is very important.

The present study aims to contribute to the existing scientific knowledge about the presence of DA on a global scale. The presence of dust, i.e., its frequency of occurrence, is important for all the phenomena and processes mentioned in the previous paragraph. It also provides information that is essential and additional to DOD, about the dust regime, while its seasonal [52] and inter-annual [53] characteristics may differ from those of dust load (DOD). An up-to-date study of the frequency of occurrence of DA is necessary since most of the existing studies about DA refer either to DOD [42,54] or to dust concentration [55,56]. On the other hand, the frequency of occurrence of DA, in particular on a global scale, has not been extensively investigated so far. Indeed, only a few studies exist,

which are spatially and temporally limited [57–59]. In addition, the few existing studies have investigated the dust frequency in terms of dust sources activation and dust storms over great dust source areas using mainly meteorological data. On the contrary, in the present study, the frequency of occurrence of DA is for the first time examined on a global basis and over an extended (15-year) period using contemporary satellite data of aerosol optical properties, providing information over all surfaces (land and ocean) at a spatial resolution of $1^\circ \times 1^\circ$ and on a daily basis. The DA's identification is achieved by using a satellite-based algorithm, which is initialized with spectral AOD data taken from MOderate Resolution Imaging Spectroradiometer (MODIS)–Aqua Collection 6.1 Level 3 dataset [60] and Aerosol Index (AI) data taken from the OMI-Aura (Ozone Monitoring Instrument) OMAER-UV dataset. The algorithm determines the dust presence all over the globe on a gridded ($1^\circ \times 1^\circ$ latitude-longitude) and daily basis over the 15-year period of 2005–2019. The monthly and the annual mean absolute and relative frequencies of occurrence of dust are computed on a pixel-level basis, enabling the study of the annual cycle of DA all over the globe (Section 3.1). Regional averages are also computed in order to more effectively examine the annual cycle of DA over specific world areas of interest, namely the world's greatest deserts (Section 3.2). Based on the algorithm runs for each month of every year of the study period, the climatological mean frequencies of DA are also calculated, and the time series of inter-annual monthly values are constructed either for the globe (Section 3.1) or the examined study regions (Section 3.2). Finally, a statistical analysis, including inter-annual trends and a Mann–Kendal test, is also conducted enabling the investigation of possible changes in DA during the study period.

2. Data and Methodology

2.1. MODIS and OMI Satellite Data

The algorithm uses the Collection 6.1 MODIS-Aqua Level-3 satellite data (product MYD08_D3). The Collection 6.1 comprises the latest of MODIS data, released in 2017, and has various refinements and improvements made to both the radiation calibration and Dark Target (DT, https://atmosphere-imager.gsfc.nasa.gov/sites/default/files/ModAtmo/C061_Aerosol_Dark_Target_v2.pdf) and Deep Blue (DB, https://atmosphere-imager.gsfc.nasa.gov/sites/default/files/ModAtmo/modis_deep_blue_c61_changes2.pdf) algorithms already used in MODIS Collection-6.0 [60]. Collection 6.1 has a better performance against the AERONET data [61–64] with respect to previous MODIS products. In the present study, spectral AOD data are taken from the MODIS C6.1, which takes advantage of the merits of the MODIS Dark Target (DT) and Deep Blue (DB) algorithms. More specifically, the C6.1 AOD data are derived from datasets produced with the MODIS Enhanced Deep Blue (DB) and DT algorithms over land and a DT algorithm over water (ocean). Over land, the AOD is available at three different wavelengths (470 nm, 550 nm and 660 nm), while over oceans, it is available at seven wavelengths (470 nm, 550 nm, 650 nm, 860 nm, 1240 nm, 1630 nm and 2130 nm). The present satellite algorithm uses these spectral AOD data to calculate the Ångström Exponent (α), which is often used as a qualitative indicator of aerosol particle size, in order to identify the presence of coarse dust aerosols. It should be noted that α is calculated for different pairs of wavelengths over land and oceans, i.e., 470–660 nm over land and 470–2130 nm over ocean, i.e., always using the smallest and longest available wavelengths. Other pairs of MODIS wavelengths were also tested in order to examine the possible sensitivity of α to them. More specifically, α was calculated for 470–660 nm over land and 470–650 nm over ocean, as well as for 550–660 nm over land and 550–650 nm over ocean. The obtained frequency distributions of dust aerosols (DA) for the indicative year 2005, which are shown in Figure S3, are very similar to each other, as well as to the wavelength pair adopted in this analysis.

The algorithm also uses Aerosol Index (AI) data, derived from measurements taken from the Ozone Monitoring Instrument (OMI) instrument onboard the NASA's EOS-Aura satellite. OMI is a compact hyperspectral nadir viewing, wide swath, ultraviolet-visible imaging spectrometer, which provides daily, high-spatial-resolution data. Its observations

are used in the retrieval of atmospheric column ozone, sulfur dioxide, nitrogen dioxide, formaldehyde and other trace gas as well as clouds and aerosols. The OMI aerosol product contains information for the AI, the AOD, and the Single Scattering Albedo (SSA), which have been evaluated with AERONET observations. In the present study, the daily Level 3 AI data of the latest OMI edition OMAERUV [65] are used.

Both MODIS and OMI products used are available on a daily and $1^\circ \times 1^\circ$ longitude–latitude resolution. The MODIS Aqua data were preferred to MODIS Terra, because Aqua and Aura are both A-train satellites, being in a polar orbit, crossing the equator within seconds or minutes of each other, thus ensuring the time collocation of the used products in the algorithm. Finally, the study period spans the 15-year period from 1 January 2005 to 31 December 2019, constrained by the simultaneous availability of both MODIS and OMI data.

It should be noted that Level 3 data, as those utilized in the present study, are appropriate for large-scale regional, and especially global-scale analyses [66,67], having the advantage of working on a regular latitude and longitude grid rather than on irregularly spaced pixels along the orbit track (Level 2 data, [68]). The only drawback of Level 3 data is that their resolution is too coarse to accurately detect small scale anthropogenic sources of dust [68], but the contribution of these sources is small compared to the contribution of the extensive physical sources of dust, namely the great desert areas.

Furthermore, it should be noted that time-averaging issues associated with Level 3 gridded products, induced by overlapping orbital tracks, may exist, only towards the poles (poleward of about 77° N), in contrast to what happens at mid-latitudes, where the time averaging issue practically does not exist (https://modis-images.gsfc.nasa.gov/_docs/L3_ATBD_C6.pdf). In particular, values from approximately 23°N to 23°S correspond to a single overpass, and they are not "daily mean values". However, even up to 60°N and 60°S, where the Global Dust Belt zone and the great world deserts are found, the 1-degree MODIS Level-3 products essentially do not involve a mixture of air masses, since they are based on either a single or two orbital swaths with a time lag of about 100 min, which corresponds to a short time for significant changes in dust to occur. It is only in higher latitudes, more poleward than 60°, that the time averaging issue induced by multiple orbits exists. However, these regions contribute a negligible amount of the global dust load.

2.2. Methodology

The satellite algorithm uses as input the MODIS spectral AOD and the OMI AI data described in Section 2.1 and determines the presence or not of DA over a specific place on a specific day. It should be noted that the utilized satellite input data are columnar and that, usually, different aerosol types co-exist in the atmospheric column. In view of this, the presence of DA should be rather taken as a predominance of dust over other aerosol types in the atmospheric column, which is reflected in the satisfaction of specific criteria ensuring the coarse size and absorbing ability of predominant dust aerosol. In a first step, the algorithm uses the spectral AOD information to calculate the α, and subsequently, it applies specific threshold values on both α and AI, as well as on AOD, to identify the presence of DA (Figure 1). These thresholds are as follows: (i) $\alpha \leq 0.4$, (ii) AI ≥ 1 and (iii) AOD ≥ 0.1. These thresholds are representative for DA, and they were selected after sensitivity tests (Figures S1–S5) and the existing literature [69–74]. These sensitivity tests show that using lower/higher AI thresholds results in larger/smaller frequencies of DA both over land and ocean and an expansion/shrinking of areas covered by DA. On the other hand, although, in general, no substantial differences appear between the results obtained for $\alpha \leq 0.4$ and $\alpha \leq 0.7$ threshold values, slightly higher frequencies of DA are found above oceanic regions, i.e., Tropical and South Atlantic Ocean, Gulf of Guinea and East Pacific Ocean. The obtained results of the algorithm using the selected thresholds confirm the presence of coarse absorbing aerosols, which is the case for DA.

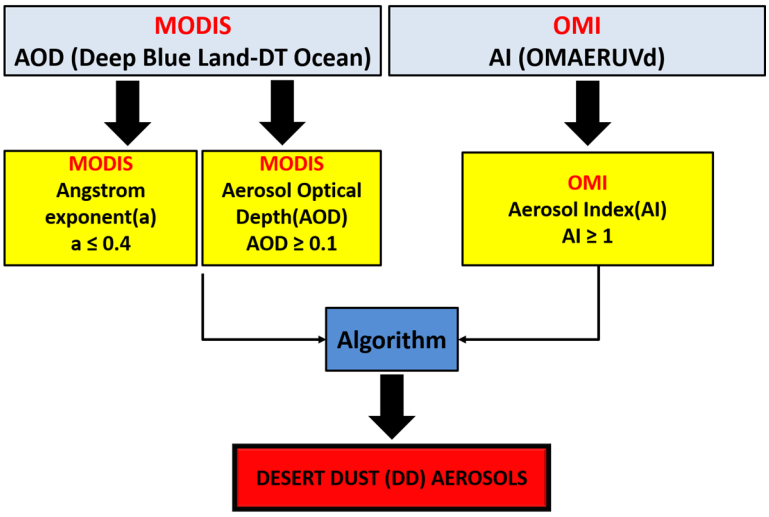

Figure 1. The satellite-based algorithm and methodology applied for the identification of dust aerosols (DA).

The algorithm identifies the presence of DA on a daily basis and subsequently calculates the frequency of occurrence of DA on a monthly and annual basis. It should be noted that apart from the absolute frequency of occurrence (N_{abs}) of DA, given in days/month or days/year, the relative frequency of occurrence (N_{rel}) is also calculated, given as a percentage of days (in a month or year) characterized by the presence of DA with respect to the number of the days (of the month or year) for which the algorithm ran. The algorithm ran for each year of the study period, producing monthly and annual mean N_{abs} and N_{rel} values, and subsequently the corresponding average 15-year (climatological) values (monthly and annual) were calculated.

Apart from temporal averages, regional monthly and annual mean absolute and relative frequencies for the globe, but also for specific world areas, namely great deserts, were also produced. The absolute frequencies result from the sum of grids over which DA were detected, while the relative frequencies were computed by dividing the number of grids with DA detected over the area of interest (region or globe) by the total number of grids of the area for which the algorithm operated. Here, it should be noted that the denominator in this calculation can be a large number since it includes a significant number of grids over which DA either are not at all or are rarely detected. In fact, this results in a lower frequency of occurrence than what would it be if the averaging was made only over grids with DA, as done in some previous studies. The selected areas of special interest with relevance to DA are those where dust aerosols are systematically the predominant aerosol type in the atmospheric column. The Sahara is such a region, being the greatest world desert and contributing more than 50% of the global dust emissions [75]. The other selected regions of interest are smaller deserts, namely the Taklamakan [43] and Gobi [76] Asian deserts and the Middle East deserts [4,44], as well as land and oceanic areas undergoing frequent transport of DD. Such areas selected in this study are the Tropical Atlantic Ocean [77–79], the Gulf of Guinea [55,80] and the Mediterranean Basin [42,81]. In the present study, ten (10) regions with a high frequency of dust occurrence are discussed. The selected world study regions are displayed in Figure 2. It should be noted that the areas of the Sahara and Tropical Atlantic are divided into East and West Sahara due to their different magnitude of dust loadings and spatial extent, as is discussed in Section 3. Similarly, Middle East area is divided into North and South Middle East.

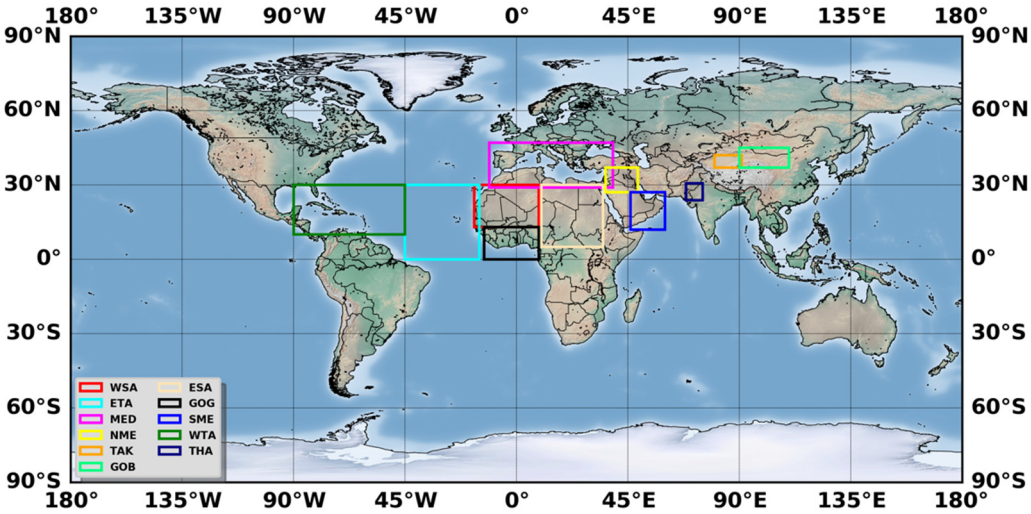

Figure 2. Geographical domains of the sub-regions considered for the regional analysis. (East Sahara (ESA), West Sahara (WSA), East Tropical Atlantic (ETA), West Tropical Atlantic (WTA), Gulf of Guinea (GOG), Mediterranean (MED), North Middle East (NME), South Middle East (SME), Thar (THA), Taklamakan (TAK), Gobi (GOB)).

3. Results and Discussion

The algorithm was applied to every day of each year of the study period of 2005–2019 and worked on a daily and 1° × 1° latitude-longitude grid-level basis. Subsequently, the monthly and annual mean global distribution of the absolute (N_{abs}) and the relative (N_{rel}) frequency of occurrence of DA were computed. The outputs were then averaged over the entire study period, yielding the 15-year averaged values, which are presented in this section.

3.1. Global Results

3.1.1. Geographical Distribution

The global distribution of the absolute annual mean frequency of occurrence of DA, expressed in number of days/year, averaged for the entire period of 2005–2019 is displayed in Figure 3a. Figure 3b displays the corresponding distribution for the DA relative frequency of occurrence, with respect to the number of days in a year for which the algorithm operated. White areas in the figures correspond to cases (grids) for which the algorithm never operated due to missing input data (non-operating algorithm). The two distributions are quite similar, indicating that the spatial patterns of the absolute frequency are not dominated by data availability. In both distributions, it is clear that the greatest part of the globe has low frequencies of DA (bluish colors) up to 5 days/year or 0.1 (i.e., 10%). Higher frequencies are observed mainly in the "global dust belt". This belt includes the greatest world deserts, namely the Sahara, Middle East, Taklamakan, Thar and Gobi deserts, expanding to the west and including a significant part of the northern Tropical Atlantic Ocean. It should be noted that relatively small frequencies are observed off the coast of Angola, in the southeastern Atlantic Ocean, not exceeding about 10% or 20 days/year. These occurrences, which take place from July to September (as shown and discussed in Figure 4) do not really correspond to the predominant presence of dust over this oceanic area. As shown by our analysis (Figure S6 and relevant discussion at the end of this subsection), they arise from the coexistence of sea-salt and biomass-burning aerosols exported from Angola. This coexistence of coarse scattering sea salt and fine-absorbing-biomass-burning aerosols, along with a weak presence of dust over this area, is misinterpreted by the present satellite algorithm, which uses columnar aerosol products as a presence of coarse-absorbing DA.

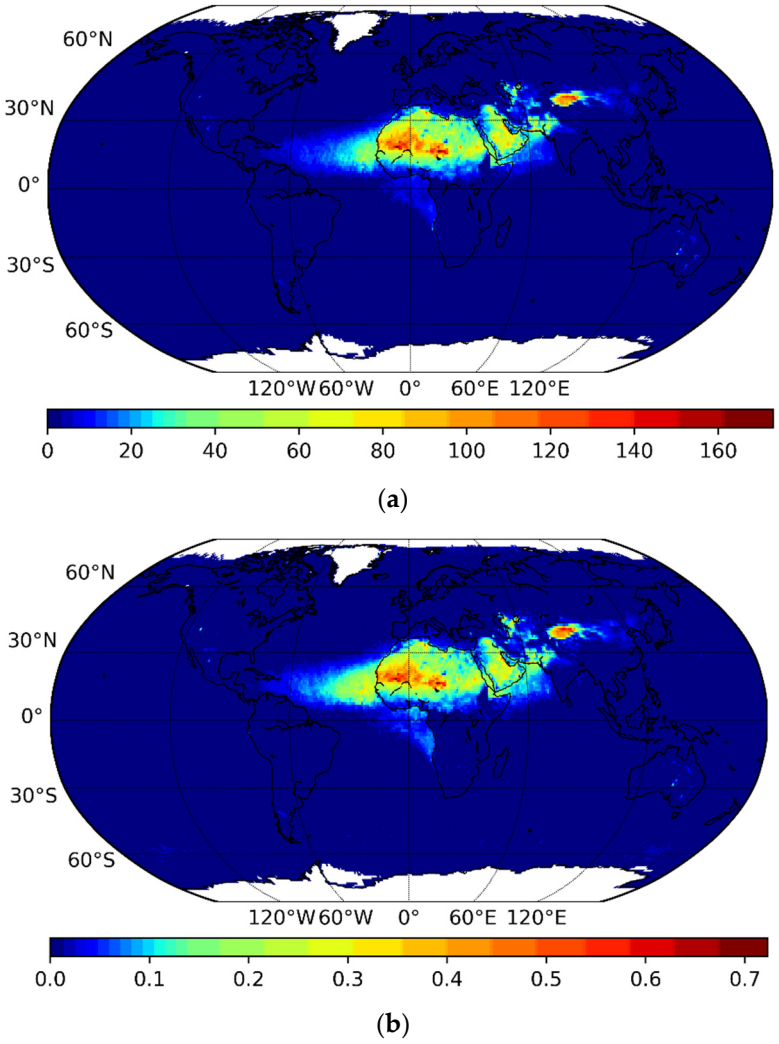

Figure 3. Global distribution of: (**a**) absolute frequency of occurrence of dust aerosols (in number of days/year); (**b**) relative percentage frequency of occurrence of dust aerosols (with respect to the number of days per year with available satellite data and for which the satellite algorithm operated). The results are averaged over the period of 2005–2019. The white-shaded areas are those for which the algorithm did not operate due to missing input data (non-operating algorithm).

The highest frequencies of DA are observed over North Africa (Sahara Desert) where the values ranged from about 60 up to 120 days/year, while in some areas (Bodélé), they are as high as 160 days/year. High frequencies are also observed over the Asian deserts Thar, Taklamakan and Gobi, with values ranging from 70–80 (greenish colors) up to 150 days/year (reddish colors), with the highest frequencies mainly observed over the Taklamakan. Quite high DA frequencies (up to 90 days/year) were observed over the Middle East, especially over its southern part, namely the Arabian desert. The frequencies of DA are generally low (up to 20 days/year) over the oceanic areas, while greater frequencies are observed only over the Mediterranean Sea (up to 30 days/year), the Arabian Sea (up to 40 days/year), the Tropical Atlantic Ocean (up to 50 days/year) and the Gulf of Guinea (up to 30 days/year).

The seasonal variation of dust aerosols is shown in Figure 4, which displays the monthly frequencies of DA averaged over the 15-year study period. Seasonal patterns are apparent only over the world great deserts and their neighboring areas, namely over the ten (10) selected areas of interest in this study (see Section 2.2 and Figure 2). These seasonal patterns, along with the inter-annual variability of DA, are discussed in detail in Section 3.2, where the regional results are presented. Below, only a brief discussion of the

seasonal variation of globally distributed DA frequency of occurrence is presented, along with the seasonal and inter-annual variation of 15-year average global DA frequencies.

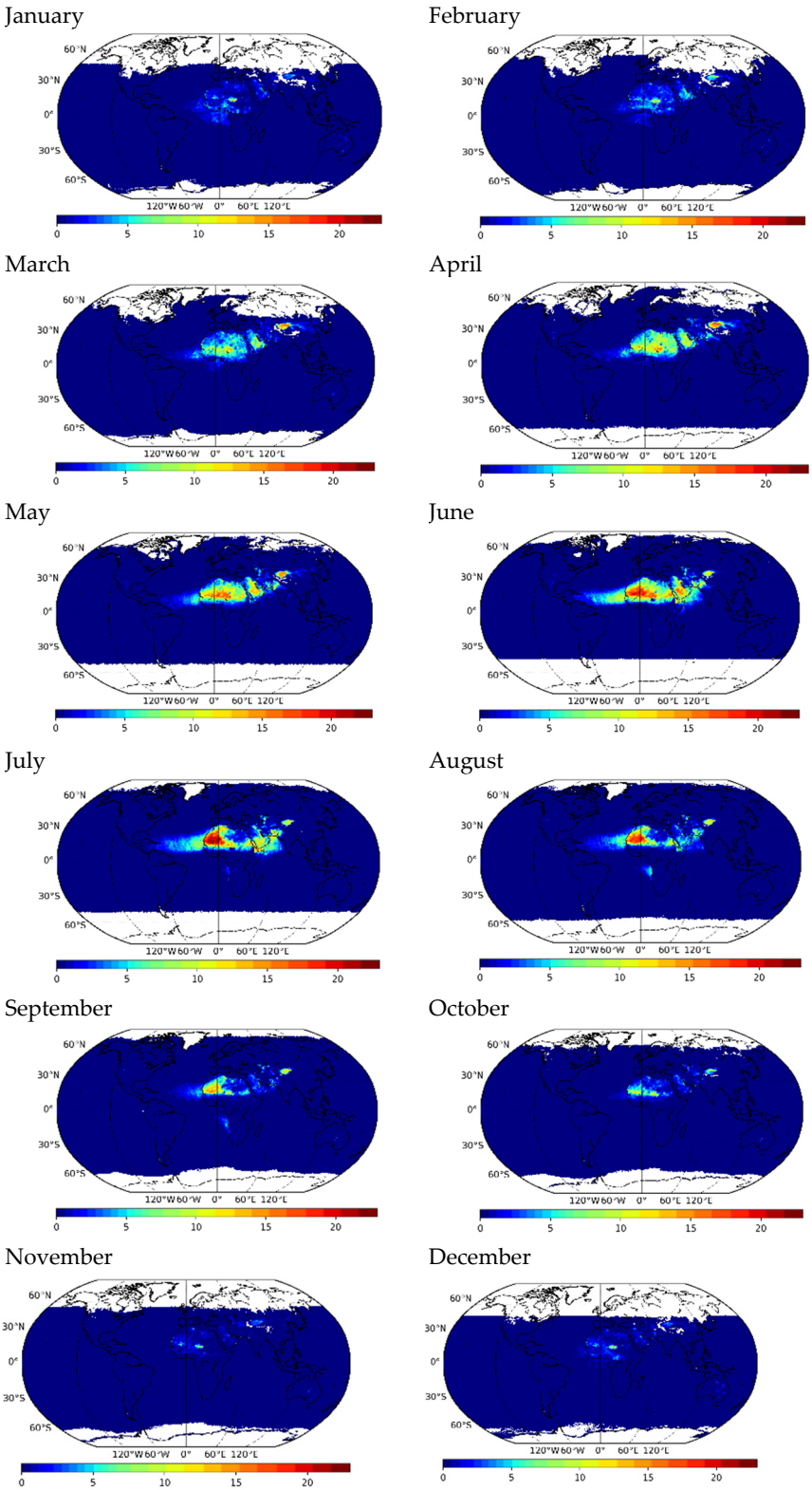

Figure 4. Global distribution of the monthly absolute frequency of occurrence of dust aerosols (in number of days/month).

Figure 4 reveals a clear seasonal cycle of DA with a remarkably stronger presence of dust in the boreal summer (especially in June) and a weaker DA presence in winter (especially in November). Although this seasonality prevails globally, it is much more pronounced over the global dust belt zone and its surrounding areas. The global dust belt zone appears more or less clearly, being expanded or shrunk in every month of the year. A latitudinal shift of this zone is notable, which is driven by the corresponding latitudinal shift of the Intertropical Convergence Zone (ITCZ). Indeed, during winter, the dust sources in southern Sahara, Sahel and sub-Sahel regions (<20°S) are well activated and combined with the blowing northeasterly (NE) Harmattan trade winds, resulting in the export of dust aerosol burden to the Gulf of Guinea [82–84]. On the other hand, during summer, the ITCZ and trade winds are shifted northwards, thus intensifying the Saharan dust sources and exporting DA to the northern Tropical Atlantic [4,82,85,86]. At the same time, the increased precipitation in the Sahel region, due to the African monsoons, decreases the airborne dust over this area [86]. During November–December–January, the largest part of the map is deep blue, indicating that the absolute frequency of dust occurrence is lower than 2 days/month. Higher frequencies of DA are observed only in January over some areas in Africa, and more specifically in the sub-Sahel region and the region north of the Gulf of Guinea, where the absolute frequency takes values up to 5–10 days/month, and especially over the Bodélé depression area, where much higher values (up to 15 days/month) are observed. The period from November to March is known as the dry or Harmattan period characterized by northeasterly trade winds over the area by high frequencies of dust occurrence [87] and dust optical depth [55,88]. In particular, Bodélé is one of the most intense dust sources in the world [4], where DA are observed all year round. Indeed, according to the algorithm results, the annual minimum frequency of DA occurrence over Bodélé, observed in November, is equal to 5–10 days/month. The DA frequencies gradually increase towards the end of boreal winter, and thus in February values up to 10 days/month are observed above the world deserts (e.g., in Northern Africa, Arabian Peninsula and Gobi).

During March–April–May, the frequencies of DA are further intensified and become more widespread. More specifically, the worldwide highest frequencies above the Sahara and Middle East deserts reach values up to 5–10 days/month in March, 7–12 days/month in April and 8–17 days/month in May. During the same period (March–April–May) the DA frequencies also increase over the Asian deserts (Thar, Taklamakan and Gobi) up to 7–15 days/month (in May). In fact, these spring frequencies are the annual maximum values over the Asian deserts, higher than the corresponding frequencies in summer, which are slightly weakened (being the maximum equal to 12 days/month). Spring maximum DA frequencies over the Asian deserts similar to those reported here (up to half days of the season) are also reported by Liu at al. (2008), who used vertically resolved data from Cloud-Aerosol Lidar and Infrared Pathfinder Satellite Observations (CALIPSO) lidar measurements. During spring, a dust transport from Asian deserts, namely Taklamakan and Gobi, towards the Pacific Ocean is noted, as indicated by light blue colors, corresponding to about 3 days/month. Such a dust transport, even reaching the western coasts of North America, has also been reported previously in the literature [43,89–91]. Dust loads and the corresponding shortwave Radiative Forcing (RF) over the West American coast were estimated by [92] using satellite data, i.e., MODIS and CERES, for three springs (namely 2004, 2005, 2006). According to their results, the mean DOD over the area is 0.1, causing a -5.51 W/m^2 shortwave RF. On the other hand, [93] provided a 10-year (2002–2011) climatology of dust aerosols over the same area, using ground-based data from the Interagency Monitoring of Protected Visual Environments (IMPROVE) network. According to their results, the climatological mean spring dust concentration was equal to 0.08–0.60 μgm^{-3}, while there is transport of DA from Asian deserts towards the Pacific Ocean. Ref. [94], using synergetic (ground-based, satellite and modeled) data, investigated two severe dust events that took place over Asian deserts and found that dust was transported to northern China, the East/Japan Sea, through to the North Pacific Ocean.

In June, the DA frequencies are even higher than in spring over North Africa (Sahara) and especially over its western part (values up to 17 days/month). These high frequencies of dust are attributed to the prevailing local pressure systems, the associated atmospheric circulation and, more specifically, the prevailing Sahara Heat Low (SHL) and west Sahara monsoon, which favor the uplift of dust. The higher DA frequencies over the western than the eastern parts of the Sahara can be explained by the easterly trade winds. Further details about this are given in the next section (Section 3.2.1). In summer, high DA frequencies are also observed over the Arabian Peninsula (up to 18 days/month) and East Sahara (up to 16 days/month), as well as over the Indo-Gangetic Plain (up to 11 days/month) and the Arabian Sea (up to 11 days/month). These results are in agreement with those reported in the existing literature [54,95–97], which are based on other datasets, e.g., European Organization for the Exploitation of Meteorological Satellites (EUMETSAT), CALIPSO, KALPANA and Indian National Satellite-3 (INSAT) 3A as well as ground-based data (from NASA's AEROsol RObotic NETwork (AERONET) and Micro-Pulse LiDAR Network (MPLNET)) and refer to shorter study periods. According to the algorithm results, during summer, and especially in June, the export of African dust to the Tropical Atlantic, which takes place since January, but to a smaller extent and with smaller intensity, is also intensified, in agreement with existing literature [77,98]. During the next two summer months, i.e., in July and August, the high DA frequencies are displaced to northwestern Africa, while the dust export to the Tropical Atlantic Ocean is also shifted slightly northwards and weakened. Finally, in September, and gradually through to the end of the year, the DA frequencies significantly and gradually decreased all over the globe, and high values (up to 16 days/month) are observed only over the deserts of North Africa and Asia.

A remarkable feature in Figure 4 is the presence of DA in the southeastern Atlantic Ocean, off the coasts of Angola, in up to 3–16 days/month during the period from July to September, maximized in August (up to 19 days/month). This appearance of DA is observed over the same location, where absorbing carbonaceous aerosols (ACA) are observed and detected by a companion version of the present algorithm [99] using the same satellite data (MODIS and OMI). These ACA are associated with an effective westward transport of African biomass aerosols originating from extensive agricultural burning and wildfires over Angola and Congo [99]. These ACA aerosols are convectively uplifted to the free troposphere and subsequently transported westward (e.g., up to the Ascension Island 2000 km offshore continental Africa) by a well-established anticyclonic circulation induced by the semi-permanent sub-tropical anticyclone of the South Atlantic [100]. The coexistence of these ACA, which are fine and absorbing, above coarse and scattering sea-salt aerosols in the underlying atmospheric layers leads to a misidentification of predominant aerosols in the atmospheric column by the present satellite algorithm. This is verified by an analysis using MERRA-2 (Modern-Era Retrospective analysis for Research and Applications, Version 2; [101]) vertically resolved (at 50 atmospheric layers from the Earth's surface up to 6 mb) extinction coefficients for five specific (5) aerosol types, namely sulfate, dust, sea-salt, black carbon and organic carbon. The obtained long-term (2005–2019) monthly mean MERRA-2 vertical aerosol profiles (Figure S6) show that indeed, from July to September, ACA, and more specifically organic carbon aerosols (red-colored curves), exist in the free troposphere (1–4 km), especially in its lowest heights (around 1000 m) overlying sea-salt aerosols (bluish curves) in the boundary layer (lower than 1000 and even more than 500 m). At the same time, the presence of DA (yellow curves) over this area and period of year is weak. It should be noted that this misidentification of DA is an inherent limitation not only of the present but of every satellite algorithm using columnar products, in cases of coexistence of sea-salt (coarse strongly scattering) and carbonaceous (fine strongly absorbing) aerosols in the atmospheric column. The only way to overcome this difficulty is to rely not on columnar but on vertically resolved aerosol products, but these are either spatially and temporally limited—for example, those from Cloud-Aerosol Lidar with Orthogonal Polarization, CALIOP onboard the CALIPSO (Cloud Aerosol Lidar and Infrared Pathfinder Satellite Observation) satellite data—or they are model driven—for

example, the MERRA-2 data, which are based on the coupled GEOS-5 (Goddard Earth Observing System, [102,103]) and GOCART (Goddard Chemistry Aerosol Radiation and Transport model, [104,105]) models.

3.1.2. Intra-Annual and Inter-Annual Cycles

The intra-annual variability of the frequency of occurrence of dust aerosols on a global basis is depicted in Figure 5, where the total number of grid cells ($1^\circ \times 1^\circ$) over which DA have been observed, in terms of averaged values over the study period 2005–2019, is given. The maximum frequency of DA is noted in June, when dust is observed over almost 23,400 pixels, i.e., over the 3.6% of the planetary surface. Note that 23,400 is the average number of grid cells over which the algorithm detected DA in June (mean value of June's cumulative DA daily frequencies over the period 2005–2019). This number is divided by the average (over the period 2005–2019) number of grid cells of the globe for which the algorithm operated during June, i.e., 633,463 grids, resulting in the low-frequency value of 3.6%. The seasonal cycle of global dust is clear, with minimum frequencies in boreal winter, taking its minimum in November, when dust is observed over only 3181 pixels or less than 1% of the planet. The error bars in Figure 5 correspond to the year-to-year (during the 15-year study period) variability of the frequency of DA on a global basis. The magnitude of variability is larger in summer (equal to about 7000 grid cells) and smaller in other seasons (minimum equal to about 3000 grid cells in November), but the existence of this year to year variability does not affect the strength of the mean annual cycle of global DA presented in Figure 5.

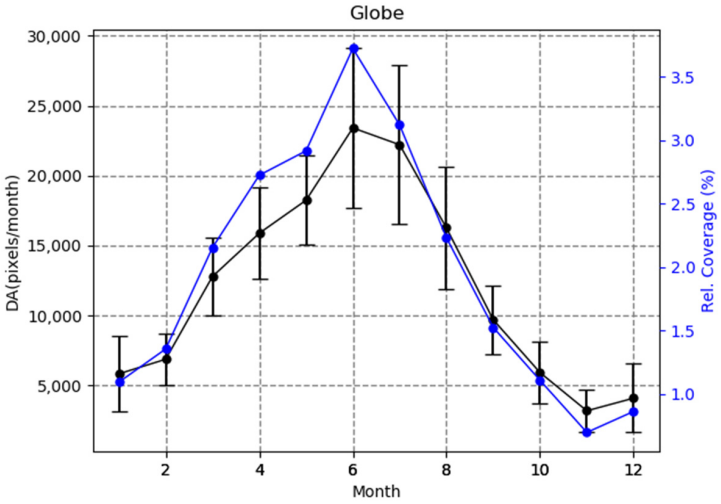

Figure 5. Intra-annual variability of the 2005–2019 averages of the global total absolute number of grid cells ($1^\circ \times 1^\circ$) where dust aerosols (DA) were detected by the satellite algorithm (left axis) and the percentage global coverage by dusty grid cells (right axis). The error bars represent the year-by-year variability by means of computed 2005–2019 standard deviations.

The inter-annual variability of the frequency of occurrence of dust on a global basis during the period 2005–2019 is shown in Figure 6, which displays the annual relative frequency of DA, expressed in terms of percentage of the area of the globe for which the algorithm operated, which (according to the algorithm) is covered by DA. A linear regression was applied to the time series of annual values in order to investigate possible changes and trends. It was found that there is a significant year-by-year variability, within the range of 0.0143–0.0290. The overall maximum frequency of dust on a global scale is observed in 2018, and the minimum in 2007 and 2009. The 2018 maximum can be associated with a minimum in global precipitation (not shown here) based on an analysis using Global Precipitation Climatology Project [106] data. In general, the presence of dust on a global basis increased from 2005 to 2019 by about 56%. This increase is statistically significant at

the 95% level, according to the applied Mann–Kendal test results, but also as ascertained from the computed standard error of the slope of the applied linear regression compared to the slope value (Figure 6).

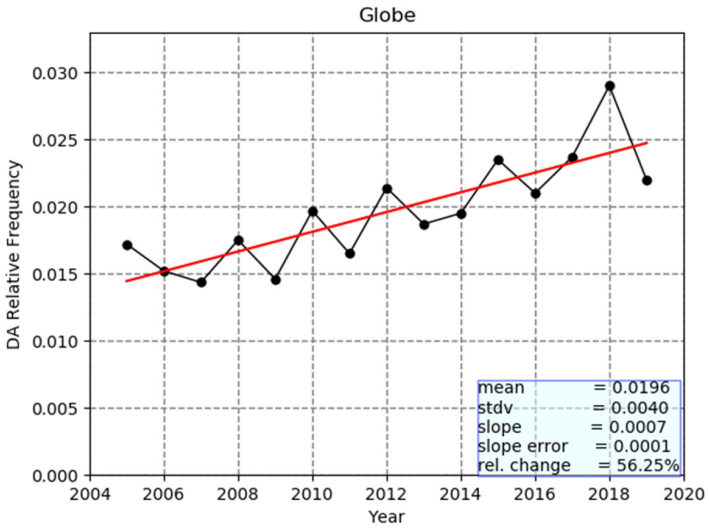

Figure 6. Inter-annual variability and linear trend of the relative frequency of dust aerosols (DA) over the globe, calculated by dividing the total absolute number of grid cells (1° × 1°) over which DA have been detected by the satellite algorithm by the total number of grids of the area for which the algorithm operated.

3.2. Regional Results

In this section, the seasonal cycle and the inter-annual variation and trends of dust aerosols over ten (10) selected world regions are discussed. For each month (intra-annual variation) or year (inter-annual variation) results are given in terms of relative frequency (sum of grid cells over which dust aerosols are observed by the satellite algorithm divided by the total number of grids of the area for which the algorithm operated, see Section 2.2). The results (statistical metrics computed for each studied region) are summarized and compared in Table 1.

Table 1. Climatological Annual Mean Relative frequency of occurrence of DA, along with the associated standard deviation, and the estimated trend over the 15-year study period (2005–2019). The relative frequency of DA is expressed in terms of the sum of grid cells over which dust aerosols (DA) are observed by the satellite algorithm divided by the total number of grids of the area for which the algorithm operated (see Section 2.2). Blue color indicates the statistically significant trend according to the applied Mann–Kendall test.

Region	Climatological Annual Mean Relative Frequency of Occurrence of DA	Relative Change (%)
East Sahara	0.1646 (±0.0394)	56.13
West Sahara	0.2937 (±0.0504)	33.11
East Tropical Atlantic	0.0980 (±0.0194)	30.00
West Tropical Atlantic	0.0303 (±0.0112)	91.81
Gulf of Guinea	0.0916 (±0.0299)	39.19
Mediterranean	0.0472 (±0.0137)	62.01
Thar	0.3241 (±0.0394)	31.97
Taklamakan	0.0511 (±0.0127)	23.59
Gobi	0.1102 (±0.0481)	21.10
North Middle East	0.1160 (±0.0404)	−2.39
South Middle East	0.1698 (±0.0429)	29.39

3.2.1. East Sahara

The eastern part of Sahara Desert (ESA, Figure 2) includes a part of Nigeria, Libya, Egypt, Sudan and Chad. In this region, the Qattarah and Bodélé depressions are also included. The latter is characterized as the most intense dust source in the world [4], with high frequencies of DA all year round, as is shown in Figures 3 and 4 (up to 170 days/year and 22 days/month). The regional results of Figure 7a reveal a clear seasonal cycle with maximum frequencies of DA in spring. The dust aerosols are observed most frequently over this region in May, covering an area of about 45,950,000 km^2, corresponding to 4595 grid cells, slightly more frequently than in April and June (4543 and 4373 grid cells, respectively). During these three months, almost 32% of the included area (Figure 7a) is covered by DA. The weakest presence of dust over East Sahara is observed in winter, and more specifically in November, when DA are observed over only less than 500 grid cells or 2.3% of the region. As indicated by the standard deviations, which are also displayed in Figure 7a and express the year to year variability, as well as the results of Figure S7ii, this seasonal cycle of DA over East Sahara is followed in every year of the study period. This seasonal cycle of DA over East Sahara can be interpreted in relation with the corresponding cycles of temperature and surface pressure. Indeed, over this region, temperature and surface pressure take lower/higher values in winter and higher/lower values in summer. These conditions favor the uplifting of dust during summer, and also the accumulation of dust aerosols during winter months (because of low wet deposition) leading to a strong presence of DA in spring, which in combination with the gradual heating of surface towards late spring and early summer, result in a late spring/early summer maximum of DA, with a drop in DA frequencies afterward.

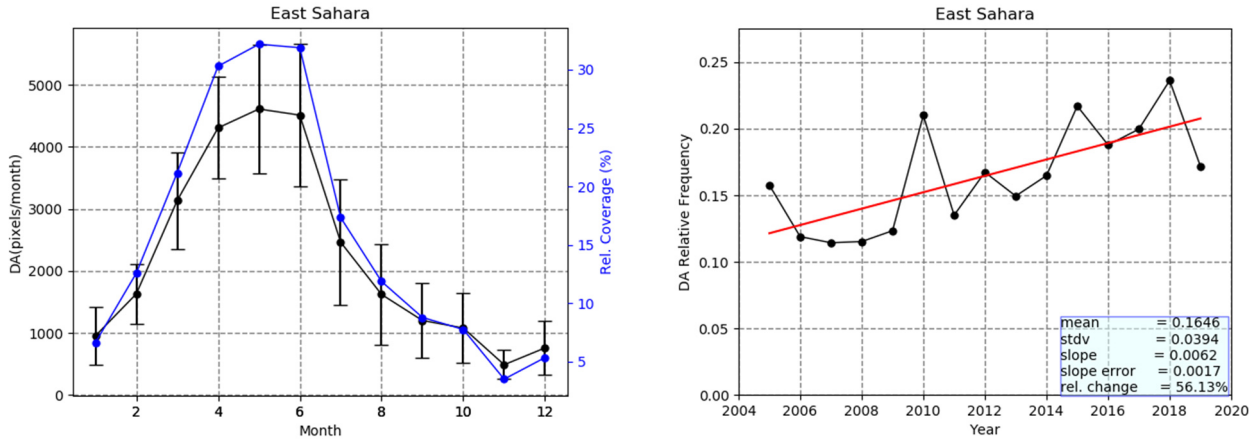

(**a**) (**b**)

Figure 7. (**a**) Intra-annual variability of the 2005–2019 averages of the total absolute number of grid cells (1° × 1°) where dust aerosols (DA) were detected over East Sahara by the satellite algorithm (left axis) and the percent coverage of the region by dusty grid cells (right axis). The error bars represent the year-by-year variability by means of computed 2005–2019 standard deviations. (**b**) Inter-annual variability and linear trend of the relative frequency of dust aerosols (DA) over East Sahara.

The inter-annual variability of dust aerosols over East Sahara is presented in Figure 7b. The annual mean values of the relative frequency of occurrence of DA vary between 0.114 and 0.236 pixels or between 11.4% and 23.6% of the region's surface area. According to the applied linear regression, a strong increase (56%) in dust presence over East Sahara during the study period (2005–2019) is observed. This increase was found to be statistically significant according to the applied Mann–Kendall test, as well as based on the computed slope error value, while it is also in agreement with published results in literature [107] covering the period 2007–2017. Despite the observed overall increasing tendency of DA during the 15-year period, two different sub-periods with opposite trends can be discerned.

More specifically, from 2005 to 2009, the frequency of occurrence of dust decreased, while it subsequently increased from 2009 to 2018. Such changes in the frequency of occurrence of dust are related with the dust transport [108] and the activation of dust sources [109].

3.2.2. West Sahara

The seasonal cycle and the magnitude of the frequency of occurrence of dust aerosols over West Sahara (WSA, Figure 2) displayed in Figure 8a is different to those for East Sahara. More specifically, the frequency of occurrence of DA is significantly higher, with values up to 6237 grid cells or 51% of the total region's surface area, compared to 4543 pixels and 32% for East Sahara. Besides, over West Sahara, high frequencies of DA occur during summer, with a maximum in July, against a dust cycle with spring maximum over East Sahara. The lowest DA frequencies over West Sahara (varying between 0 and 500 grid cells) are observed in November, December and January. As indicated by the magnitude of error bars in Figure 8a and also by the results of Figure S7iii displaying the annual cycle of DA for every year, the month with the lowest frequency of DA varies, depending on the year, within November, December and January. The seasonality of dust aerosols over West Sahara is driven by Harmattan winds, SHL and the west Sahara monsoons, which blow in the area from the Gulf of Guinea, transporting cold and moist air masses. The prevailing atmospheric conditions (monsoons and SHL) favor convection and as a consequence the uplift of dust and its transport to the upper atmosphere. Once dust is introduced into the atmosphere, it is transported to other regions, namely the Tropical Atlantic Ocean, driven by the atmospheric circulation and especially the Harmattan winds.

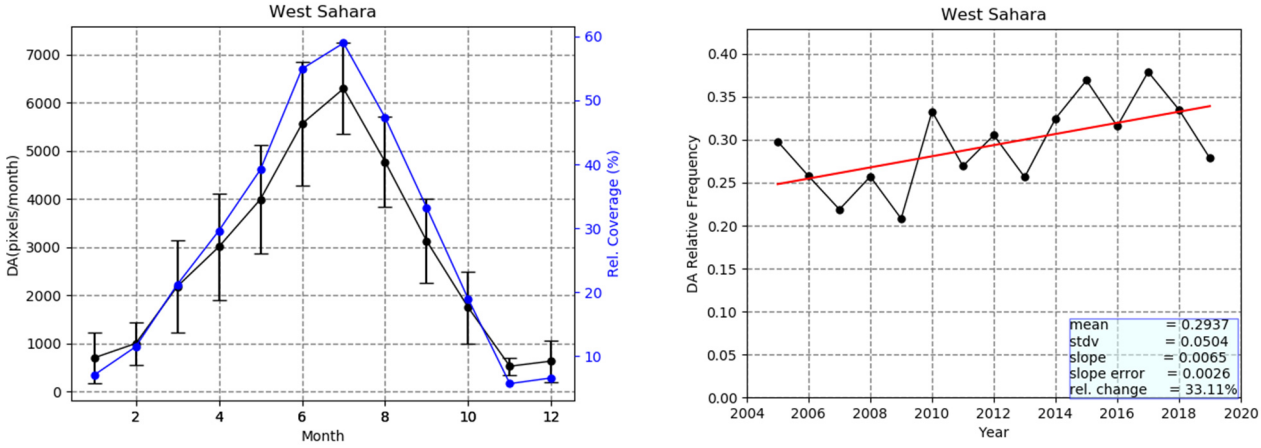

Figure 8. (**a**) Intra-annual variability of the 2005–2019 averages of the total absolute number of grid cells (1° × 1°) where dust aerosols (DA) were detected over West Sahara by the satellite algorithm (left axis) and the percent coverage of the region by dusty grid cells (right axis). The error bars represent the year-by-year variability by means of computed 2005–2019 standard deviations. (**b**) Inter-annual variability and linear trend of the relative frequency of dust aerosols (DA) over West Sahara.

The inter-annual variability of dust aerosols occurrence over West Sahara (Figure 8b) displays several ups and downs, with annual mean values ranging from 0.2082 (2009) to 0.3789 (2017). An increasing trend (33.1%) is ascertained by the applied linear regression, which according to the applied Man-Kendall test is statistically significant at the 95% level. Similar to the case of East Sahara, the overall linear trend over the entire study period (2005–2019) can be split into two sub-periods with different tendencies: (a) the period of 2005–2011, characterized by a decreasing tendency, and (b) the period 2011–2019, characterized by an increasing tendency.

3.2.3. East Tropical Atlantic Ocean

As described in the previous sections, dust aerosols can be transported far away from their source areas. This is the case of the Tropical Atlantic Ocean (ETA, Figure 2), where high loads of dust arrive from the Sahara desert, driven by the Harmattan winds, and more specifically by the interaction between the Harmattan winds and the moist west African summer monsoon, producing west African thunderstorms [8,77,78,85,86]. This phenomenon takes place every (boreal) summer, typically between April and November, with different intensity and spatial extent [58,77], leading to dust transport as far as the Caribbean basin [110].

The seasonal variability of the frequency of occurrence of dust over the East Tropical Atlantic Ocean (Figure 9a) reveals a quite clear cycle with a primary maximum in June. This seasonal cycle, also reported in the literature [8,58,78,86], is very similar to the corresponding seasonal cycle for West Sahara (Figure 8a). This is reasonable since dust over the East Tropical Atlantic Ocean originates mainly from central and western Sahara [8,79,86]. However, the comparison between Figures 8a and 9a shows that the frequency of DA is lower over the East Tropical Atlantic Ocean (with values ranging from 153 to 2998 grid cells) than the West Sahara (with values between 550 and 6237 grid cells). It should be noted that standard deviations in Figure 9a (East Tropical Atlantic Ocean) indicate a significant year-to-year variability of DA (also depicted in Figure S7iv), which is quite larger than that in Figure 8a (West Sahara). This, given that West Sahara is the source of dust over the East Tropical Atlantic Ocean, suggests that the larger year-by-year variability of dust over the East Tropical Atlantic Ocean is not only due to a similarly stronger inter-annual variability of dust sources and emitting mechanisms but is also associated with phenomena that drive or influence dust transport [77]. In Figure 9a, apart from the summer maximum in June, a secondary, but much smaller, maximum is also observed in spring (March–April). This maximum can be attributed to dust transport from the eastern Sahara, where dust emissions are maximum in these months (Figure 8a). Indeed, it has been reported in the literature [111] that a great part of dust aerosols in the Tropical Atlantic originates from the Bodélé depression, which is located within the East Sahara study region (Figure 2).

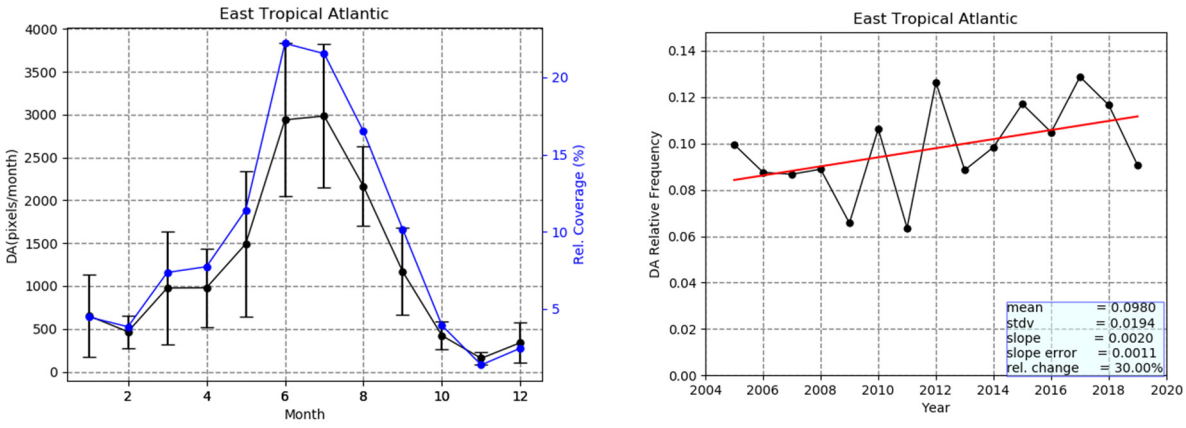

(**a**) (**b**)

Figure 9. (**a**) Intra-annual variability of the 2005–2019 averages of the total absolute number of grid cells (1° × 1°) where dust aerosols (DA) were detected over East Tropical Atlantic by the satellite algorithm (left axis) and the percent coverage of the region by dusty grid cells (right axis). The error bars represent the year-by-year variability by means of computed 2005–2019 standard deviations. (**b**) Inter-annual variability and linear trend of the relative frequency of dust aerosols (DA) over East Tropical Atlantic.

The inter-annual variability of dust occurrence over the East Tropical Atlantic Ocean is relatively small (values ranging from about 0.0635 in 2011 to 0.1288 in 2017, Figure 9b) and smaller than over the Sahara (West and East). The results also indicate that the occurrence of DA increased during the study period by 30%. This trend is not statistically significant at

the 95% level according to the applied Mann–Kendall test, but it is statistically significant based on the computed slope error value). The inter-annual variability (similarly to the seasonal one) of DA over the East Tropical Atlantic Ocean is in quite good agreement with the corresponding variability over Sahara (East and West), revealing a decrease from 2005 to 2011, followed by a subsequent increase until 2018. Figures 7b, 8b and 9b show that there has been an increase of DA during the period of 2005–2019, which gets smaller moving westwards, towards the North African coasts and the adjacent East Tropical Atlantic Ocean. This may be attributed to dust removal mechanisms (wet and dry deposition) as well as to changes in atmospheric phenomena, such as the North Atlantic Oscillation (NAO). Indeed, Ref. [77] found a strong correlation between winter Dust Optical Thickness (DOT) over Northern Tropical Atlantic Ocean and NAO Index (NAOI) (correlation coefficients r = 0.67 and r = 0.74, for TOMS and Meteosat DOT, respectively, from 1984 to 1997). This correlation is even stronger than that reported by [111] for summer using Meteosat data for the period 1984–1994. A similar correlation between dust frequency (DA) and NAOI was found in the present study. More specifically, r values equal to 0.59 and 0.32 were found for winter and summer, respectively. It is also noted that results from a correlation analysis between DOD and NAOI (not shown here) yielded r values equal to 0.47 and 0.35 for winter and summer, respectively.

3.2.4. West Tropical Atlantic

The intra-annual variability of dust aerosols over the West Tropical Atlantic Ocean (WTA, Figure 2) shown in Figure 10a exhibits the same annual cycle with that for the East Tropical Atlantic Ocean, as well as for the West and East Sahara areas, which are the main dust source areas for the Tropical Atlantic. However, as expected, because of the westward transport of African dust, the frequencies of occurrence of dust in this region are further decreased, with respect to those in the East Tropical Atlantic Ocean, varying between 19 grid cells in February and 1095 pixels in July or, in terms of regional surface area coverage by dust, from 0.07% to 11%. The weakened presence of DA over the western than the eastern part of the Tropical Atlantic Ocean is attributed to the gradual deposition of dust (e.g., dry deposition including gravitational settling or wet deposition associated with precipitation and cloud scavenging [112]). The weak presence of dust over the West Tropical Atlantic Ocean is not strange, given the long distance from the Sahara (actually, the western limit of the region is the Caribbean Sea, located 7000 km from the dust source [110]). A noticeable characteristic in Figure 10a is the strong year-by-year variability of the DA's frequency (as indicated by the large error bars in Figure 10a and the diversity of annual curves in Figure S7v). This shows that the dust transport, done by the trade winds and maximized in summer, as well as the dust deposition (wet and dry), vary significantly from year to year, resulting in a strong inter-annual variability. This is also shown in Figure 10b, which displays the series of annual mean frequencies of DA over the study region from 2005 to 2019. On an annual basis, at the West Tropical Atlantic, the frequencies vary between 0.0122 (in 2011) and 0.0518 (in 2018). The applied linear regression and the Mann–Kendall test, but also the computed slope error value, reveal a statistically significant increase in DA during the 15-year study period, equal to 91.8%. This increase, as expected, is in line with the already discussed increase in DA over the East Tropical Atlantic Ocean and the West and East Sahara regions. Of course, the inter-annual tendency of DA over the West and East Tropical Atlantic Ocean does not only depend on the West and East Sahara source regions, but also on the DA transport mechanisms. The identified increase in DA over the West Tropical Atlantic is in line with as well as with increasing NAOI during the study period. Ref. [113] connected the AOD anomaly over the Tropical Atlantic Ocean not only with NAO, but also with ENSO. More specifically, they distinguished between summer (June–July–August) and winter (December–January–February) anomalies, and they associated the summer anomalies with ENSO (r values up to about 0.6–0.7 on a localized grid cell level basis) and the winter anomalies with NAO (r values up to about 0.4, again on a grid cell level basis). On the other hand, Ref. [114] correlated modeled

anomalies of summer dust concentration data over the 1965–2008 period with Multivariate ENSO Index (ENSOI) in Barbados and reported an r value equal to 0.20. Here, a correlation coefficient equal to 0.17 was found between summer DA anomalies and ENSOI, whereas a correlation coefficient of 0.12 was found between winter DA anomalies and NAOI. The lower r values in our analysis than those reported by [113] are explained by the fact that our correlation is done using regional DA values averaged over a region in which the r values reported by [113] range from slightly negative up to 0.6 values. It should also be noted that in the present study, the correlation with NAOI and ENSOI is done using DA frequencies, whereas in the other two studies, AOD and dust concentration were correlated with NAOI and ENSOI.

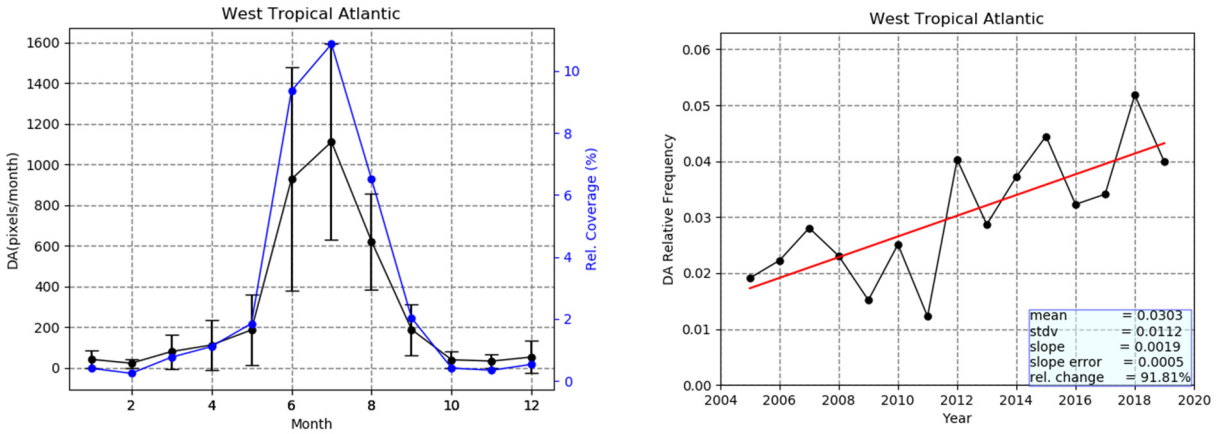

Figure 10. (**a**) Intra-annual variability of the 2005–2019 averages of the total absolute number of grid cells (1° × 1°), where dust aerosols (DA) were detected over West Tropical Atlantic by the satellite algorithm (left axis) and the percent coverage of the region by dusty grid cells (right axis). The error bars represent the year-by-year variability by means of computed 2005–2019 standard deviations. (**b**) Inter-annual variability and linear trend of the relative frequency of dust aerosols (DA) over West Tropical Atlantic.

3.2.5. Gulf of Guinea

Apart from the Tropical Atlantic Ocean, desert dust from Sahara is also transported to the Gulf of Guinea (GOG, Figure 2) [55,88,115]. More specifically, during (boreal) winter, when the ITCZ is shifted to the equator, trade winds take a strengthened northeastern direction and transport dust aerosols towards the Gulf of Guinea. Indeed, during winter, 60% of the Sahara desert's DA reach the Gulf of Guinea [80]. On the other hand, during boreal summer, the ITCZ shifts northwards, resulting in eastern trade winds over Sahara, leading to dust export to the Tropical Atlantic Ocean and not to the Gulf of Guinea. This seasonal change in the position and direction of trade winds results in a seasonality of dust over the Gulf of Guinea, which is nicely depicted in Figure 11a. There is a clear annual cycle of DA, with maximum frequencies in winter (December to March, up to 861 grid cells) and minimum in late summer and autumn (August to October, down to 53 grid cells). This seasonal variability of dust is associated not only with trade winds but also with precipitation. During winter, the precipitation amount over the Gulf of Guinea is low (less than 0.5 mm/day, [116]), and the soil of the sub-Saharan Africa (Sahel and sub-Sahel) is arid, so the Harmattan winds transport big quantities of dust to the study region [55]. On the other hand, during summer (when southern winds and monsoons prevail in the region) the amount of precipitation is higher (5–19 mm/day, [116]), and thus the regional dust load is decreased. The year-to-year variability of dust over the Gulf of Guinea is significant, especially in winter, as indicated by the size of error bars as well as by the great variability of winter frequencies of DA over the region from one year to another (see Figure S7vi). Besides, the year-to-year variability of annual frequencies of DA (Figure 11b) is considerable (values within the range 0.0520–0.1483), while there has been an increasing

trend (39.2%) during the 15-year study period, which is however not statistically significant according to the applied Mann–Kendal test, but it is so according to the slope error value.

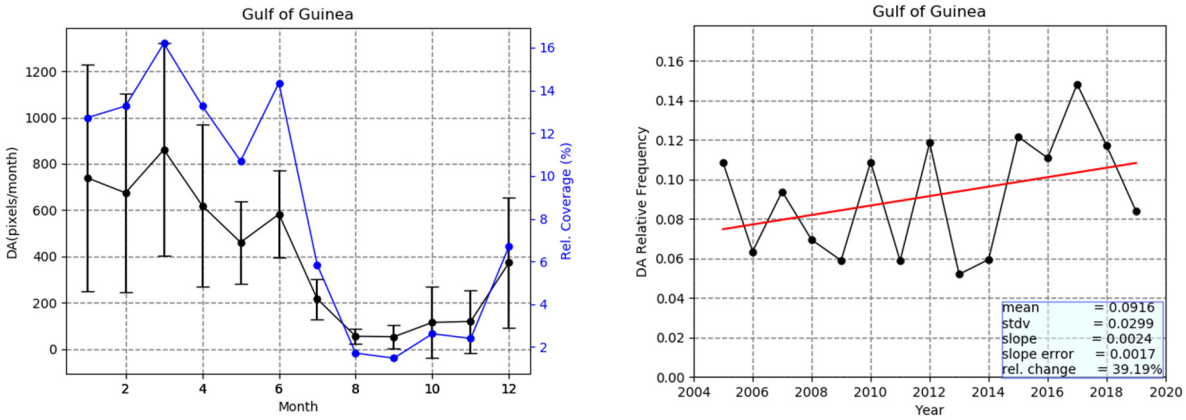

(**a**) (**b**)

Figure 11. (**a**) Intra-annual variability of the 2005–2019 averages of the total absolute number of grid cells (1° × 1°) where dust aerosols (DA) were detected over Gulf of Guinea by the satellite algorithm (left axis) and the percent coverage of the region by dusty grid cells (right axis). The error bars represent the year-by-year variability by means of computed 2005–2019 standard deviations. (**b**) Inter-annual variability and linear trend of the relative frequency of dust aerosols (DA) over Gulf of Guinea.

3.2.6. Mediterranean Basin

The Mediterranean Basin (MB) (MED, Figure 2) located near the greatest world deserts, is one of the most interesting areas with relevance to dust aerosols. DA are transported to the region mainly from Sahara Desert in North Africa, but also from Middle East, under favorable atmospheric conditions [117]. The algorithm results (Figure 12a) indicate that the presence of dust over the MB follows an annual cycle with two maxima. The primary maximum occurs in summer, and more specifically in July, when dust covers 1664 grid cells/month or 7.8% of the surface area of the MB. A secondary maximum occurs in spring (April), corresponding to 1151 grid cells/month or 7% of the regional surface area. According to the existing literature [74] but also the algorithm results, these two maxima arise from different parts of the Mediterranean Basin. The primary summer maximum is attributed to dust transport from the central–western Sahara to the Western Mediterranean, driven by the coexistence of a low-pressure system over the central–western Sahara and a high-pressure system over the eastern Sahara [58]. On the other hand, the secondary spring maximum is related to African dust transport mainly to the central, but also to the eastern Mediterranean, caused by moving low pressures over the Sahara (spring Sharav cyclones, [118]). The time series of mean annual values of DA's frequency over the Mediterranean Basin (Figure 12b) indicate that dust covers from 2.02% up to 7.07% of the study area. The observed inter-annual variability is attributed to changes in the produced dust (from sources that are mainly located in North Africa) as well as changes in dust transport [117] and deposition (e.g., precipitation [119]) mechanisms. For example, the high frequencies of dust observed in 2008 are associated with a high number of active dust sources and strong cyclonic circulation over North Africa in this year [109]. On the other hand, the very high DA frequency in 2018 (highest over the 15-year study period) is related to reduced precipitation and remarkable south-southwestern wind directions over the eastern Mediterranean Basin (cyclonic circulation) and strong winds over N. Africa [120]. The North African dust transport to the Mediterranean is associated with the North Atlantic Oscillation (NAO) and more specifically with the positive phase of NAO [111,121]. Such conditions cause drier winters in the MB [119,122] and, as a consequence, they reduce the dust wet deposition [111,123]. The relationship between NAO and dust over the MB is verified by the algorithm results, which show an increasing trend (statistically significant

according to the applied Man Kendall test and according to the computed slope error value) of DA's occurrence (equal to 62%) during the study period, which coincides with a corresponding increasing trend in North Atlantic Oscillation Index (NAOI).

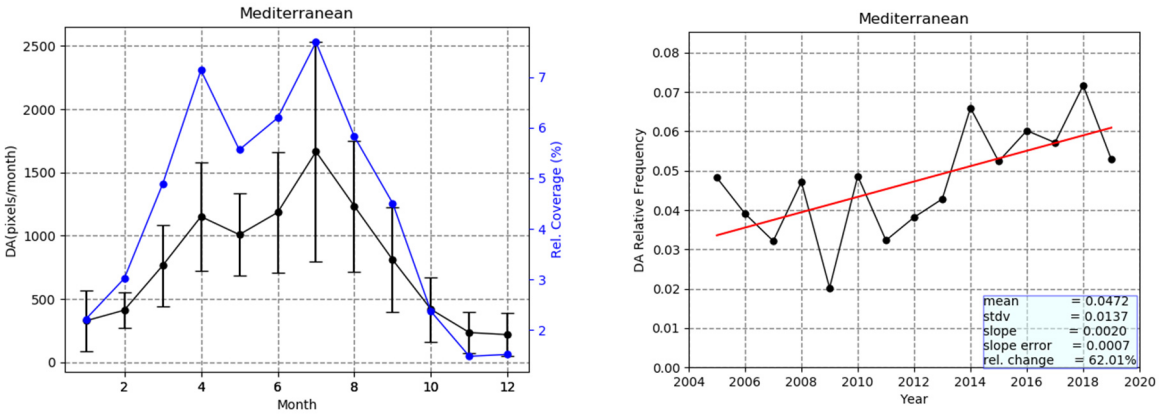

(**a**) (**b**)

Figure 12. (**a**) Intra-annual variability of the 2005–2019 averages of the total absolute number of grid cells (1° × 1°) where dust aerosols (DA) were detected over Mediterranean by the satellite algorithm (left axis) and the percent coverage of the region by dusty grid cells (right axis). The error bars represent the year-by-year variability by means of computed 2005–2019 standard deviations. (**b**) Inter-annual variability and linear trend of the relative frequency of dust aerosols (DA) over the Mediterranean.

3.2.7. Taklamakan Desert

The Taklamakan desert (TAK, Figure 2) is an important dust source, which provides the atmosphere with approximately 200 Tg of dust per year [23]. According to the existing literature, dust emissions in the area are maximum during spring months, after the dry season (minimum precipitation in winter, [96]) and during the strongest uplifting [124]. On the other hand, dust emissions become minimum during winter (November–December–January) after the rainy monsoon period and when downward vertical winds prevail [23,59,124,125]. These seasonal patterns of dust emission are in line with the average intra-annual variability of dust over the Taklamakan desert, estimated by the algorithm (2005–2019). Indeed, the results displayed in Figure 13a show a distinct maximum in spring (April) equal to 791 grid cells/month corresponding to a 56% coverage of the Taklamakan study area by DA. Apart from the primary spring maximum of DA, a secondary one in summer is also observed (447 grid cells/month and 34% coverage) which may be attributed to the maximum upward vertical wind velocities prevailing during this season [124]. The inter-annual variability of the frequency of occurrence of DA over Taklamakan (Figure 13b and Figure S7vii) does not show a significant year by year variation (values ranging from 0.2430 to 0.3809). The applied linear regression reveals a considerable (equal to 23.6%) statistically significant, according to the Mann–Kendal test and also according to the computed slope error value, increase in DA's occurrence during the 15-year period of 2005–2019.

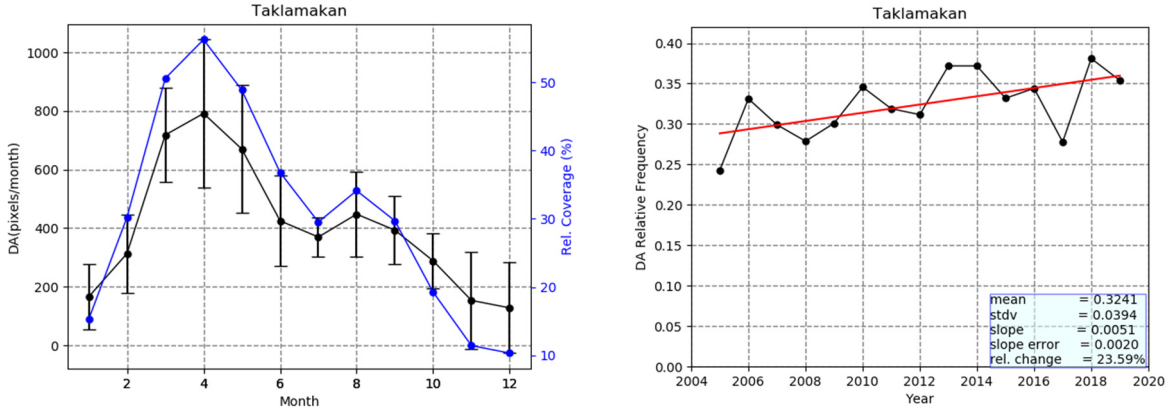

Figure 13. (**a**) Intra-annual variability of the 2005–2019 averages of the total absolute number of grid cells (1° × 1°) where dust aerosols (DA) were detected over Taklamakan by the satellite algorithm (left axis) and the percent coverage of the region by dusty grid cells (right axis). The error bars represent the year-by-year variability by means of computed 2005–2019 standard deviations. (**b**) Inter-annual variability and linear trend of the relative frequency of dust aerosols (DA) over Taklamakan.

3.2.8. Gobi Desert

The Gobi Desert (GOB, Figure 2) is located in northern China and southern Mongolia, near the previously discussed Taklamakan desert (Figure 2). Although these two great Asian deserts have a quite similar annual cycle of DA, there are slight differences between them. The Gobi has just a single spring maximum, in April (470 grid cells/month and 15% areal coverage, Figure 14a) and not a secondary one in summer, as the Taklamakan does. The same seasonality of DA occurrence over the Gobi was also found by [23], who investigated the spatial and temporal characteristics of dust in East Asia, using vertically resolved CALIPSO data for the period of January 2007–December 2011. The lower dust frequencies over the Gobi than the Taklamakan can be attributed to the higher precipitation in the Gobi compared to the Taklamakan [116]. Concerning the inter-annual variability of dust over the Gobi (Figure 14b), it was found, again, that it is very similar to that of the nearby Taklamakan desert. For example, peaks in 2006, 2010, 2014 and 2018 are observed for both deserts, exhibiting a notable 4-year periodicity. The range of variability of the annual DA frequency is smaller in absolute terms over the Gobi than the Taklamakan (0.0327–0.0729 against 0.2430–0.3809, respectively), but it is larger in relative percent terms (79% against 43%). Such a stronger variability of dust emission and transport over the Gobi than the Taklamakan has also been reported by [59], who used MISR satellite observations and trajectory analysis for the period of 2001–2011, and it is attributed to the complicated meteorological conditions (and especially the frontal activity) over the Gobi [126]. The applied linear regression indicates an increasing (21.1%) but not significant (according to the Mann–Kendall test and the computed error slope value) trend of DA during the period 2005–2019, which is smaller than the corresponding estimated increase for the Taklamakan desert. It should be noted that the estimated increase of the frequency of occurrence of dust over the Gobi is in line with the results published in the literature [127–129].

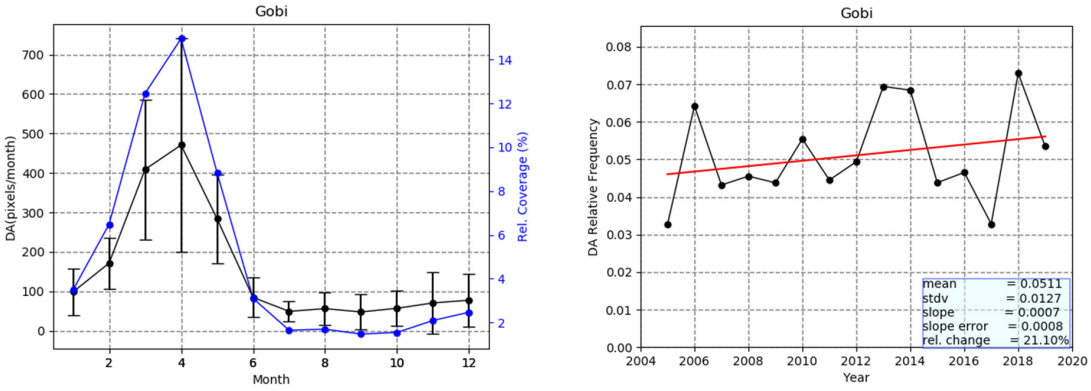

Figure 14. (**a**) Intra-annual variability of the 2005–2019 averages of the total absolute number of grid cells (1° × 1°) where dust aerosols (DA) have been detected over the Gobi by the satellite algorithm (left axis) and the percent coverage of the region by dusty grid cells (right axis). The error bars represent the year-by-year variability by means of computed 2005–2019 standard deviations. (**b**) Inter-annual variability and linear trend of the relative frequency of dust aerosols (DA) over Gobi.

3.2.9. Thar Desert

The Thar Desert is located in the northwestern part of the Indian subcontinent (Figure 2) and is one of the major Asian dust sources, characterized by extremely dry conditions (rainfall < 0.5 mm/year, Adler et al. 2003) and the absence of vegetation. The intra-annual variability of DA frequency of occurrence in this region is influenced by the South Asian monsoon (June to September, [130]). As observed in Figure 15a, the frequency of DA is maximum in late spring and early summer (dry period), when dust dominates over more than 30% of the region's surface area. On the other hand, dust emissions become minimum over the area after the wet period (October to January), when, according to the algorithm, the DA frequency is almost zero. Regarding the inter-annual variability of the DA frequency, the results of the algorithm indicate a slight increase during the study period (2005–2019). However, this increase is not statistically significant neither according to the applied Mann–Kendal test nor according to the slope error value. A decrease in dust activity in the region, connected with an increase in precipitation, has been reported in the literature [131,132], but it should be noted that these previous studies refer to DOD and not to the frequency of dust occurrence, which is the case here. In addition, and this might be more important, these studies do not include 2018, which is a dusty year that strongly influences the estimated trend. Indeed, when the last two years, 2018 and 2019, are excluded, the trend turns to be slightly decreasing (−9.5%).

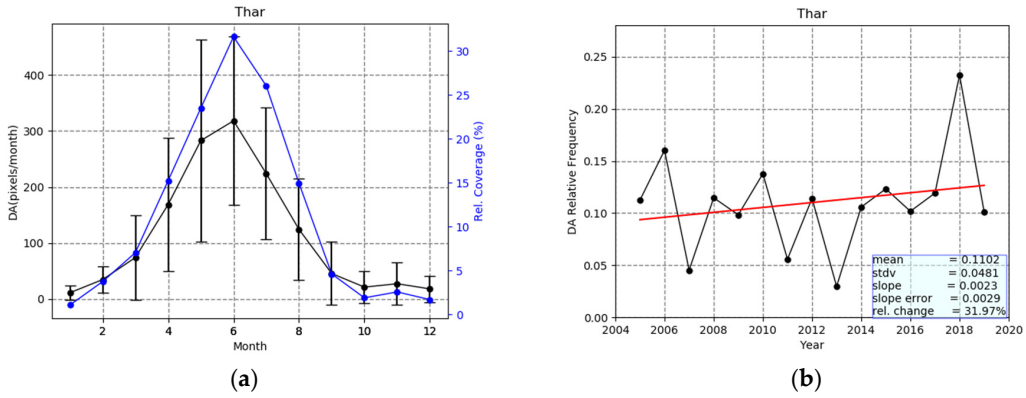

Figure 15. (**a**) Intra-annual variability of the 2005–2019 averages of the total absolute number of grid cells (1° × 1°) where dust aerosols (DA) were detected over the Thar desert by the satellite algorithm (left axis) and the percent coverage of the region by dusty grid cells (right axis). The error bars represent the year-by-year variability by means of computed 2005–2019 standard deviations. (**b**) Inter-annual variability and linear trend of the relative frequency of dust aerosols (DA) over Thar.

3.2.10. North Middle East

According to the algorithm results, dust aerosols are most frequently observed over the North Middle East desert (NME, Figure 2) from March to July, with a peak in May (Figure 16a, 729 grid cells/month), when they cover 21% of the total surface area of the region. On the contrary, during winter, their frequency is reduced and becomes minimum in November (92 grid cells/month or 2% of the regional surface area). Nevertheless, the large year-to-year variability (large error bars in Figure 15a and diversity of annual curves of DA frequency in Figure S7x), indicating a great year-by-year variability, partly reduces the certitude of the aforementioned annual cycle of DA. This seasonal variability of dust over North Middle East agrees with previous studies, such [45], based on ground-based and satellite observations as well as model simulations, covering the period 2004–2008. The algorithm results show that dust is observed throughout the year. Indeed, it is known that low altitude, soil erosion (due to cultivation and deforestation) and the Tigris and Euphrates rivers, which bring sediments in the region, are some of the factors making North Middle East an important dust source [4,44]. In addition, dust over North Middle East originates not only from regional sources (e.g., Iraq) but also from northern Africa [130] through cyclonic circulation occurring above the northern Middle East and the eastern Mediterranean Basin [133]. Figure 16b reveals that there is great year-by-year variability of dust, with annual mean frequencies ranging from 0.0499 to 0.1638. A strong dust activity is observed during the period of 2008–2012, which is suppressed in the subsequent years. The applied linear regression results in a weak decrease (−2.4%), which is not statistically significant according to either the Mann–Kendall test or the slope error value. This variability of dust over North Middle East has been associated with phenomena such as the Southern Oscillation (SO). Thus, Ref. [97] found that during positive phases of SO (La Nina) stronger vertical winds, causing dust uplift, prevail over the Arabian Peninsula unlike the negative phases of SO (El Nino). SO is described by the Multivariate ENSO Index, which takes positive values during El Nino and negative during La Nina. Indeed, during the period 2008–2012, when high frequencies of DA are observed over North Middle East, the Multivariate ENSO Index values were strongly negative (https://psl.noaa.gov/enso/mei/). The linearly decreasing frequency of DA over North Middle East during the period of 2005–2019 is also in line with increasing values of Multivariate ENSO Index over the same period (results not shown here).

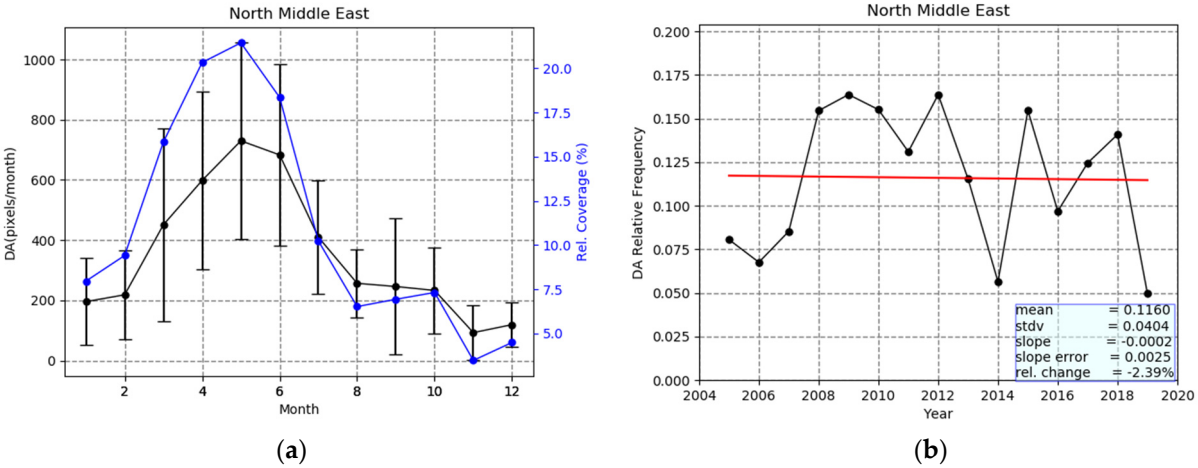

Figure 16. (**a**) Intra-annual variability of the 2005–2019 averages of the total absolute number of grid cells (1° × 1°) where dust aerosols (DA) were detected over North Middle East by the satellite algorithm (left axis) and the percent coverage of the region by dusty grid cells (right axis). The error bars represent the year-by-year variability by means of computed 2005–2019 standard deviations. (**b**) Inter-annual variability and linear trend of the relative frequency of dust aerosols (DA) over North Middle East.

3.2.11. South Middle East–Arabia

The maximum frequencies of occurrence of dust over the South Middle East desert (SME, Figure 2) are observed a bit later than over the North Middle East desert, namely in June (Figure 17a, 1903 grid cells/month, corresponding to 41% of the total surface area of the region). Such a seasonal variation has been reported by [4] but referring to the period 1980–1992 and was claimed to be connected to the prevailing sea-level pressure and updraft motions as well as to precipitation and soil moisture [134]. Indeed, during winter, the region is under the prevalence of the Siberian high-pressure system, while in summer it is affected by the Pakistan heat low favoring convection. On the other hand, precipitation is minimum in summer and higher in winter (maximum in spring, [116]). The inter-annual variability of the frequency of occurrence of dust (Figure 16b) reveals higher annual mean values and stronger year-by-year variability (0.1093–0.2463 versus 0.0497–0.1638) compared to the North Middle East desert. Dust activity in the region has been reported to be connected to ENSO. More specifically, Ref. [97] found that during El Nino (negative phase) the dust optical depth is reduced, while during La Nina it is increased. The applied linear regression to the time series of annual mean frequencies reveals a not statistically significant at the 95% level increasing trend (29.4%) according to the Mann–Kendall test, but marginally significant according to the computed slope and slope error values.

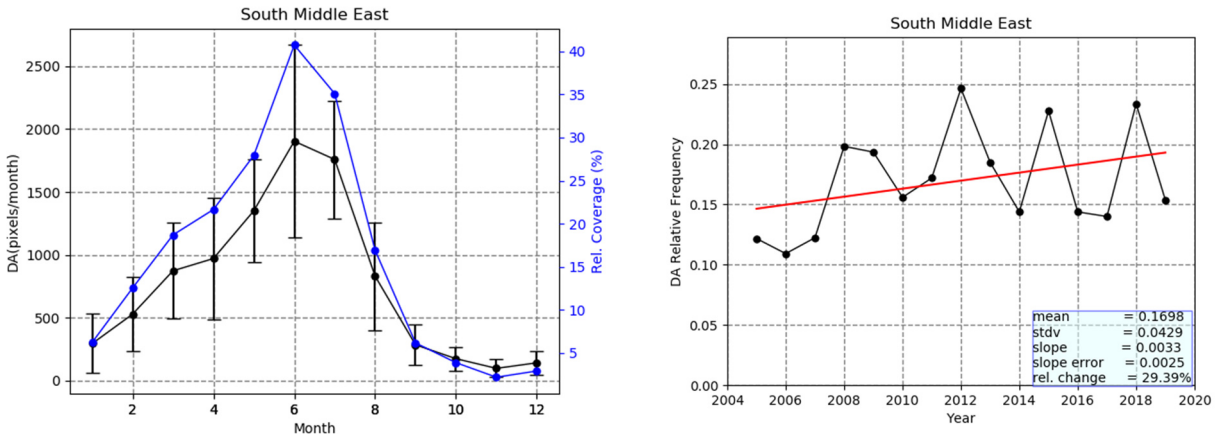

(**a**) (**b**)

Figure 17. (**a**) Intra-annual variability of the 2005–2019 averages of the total absolute number of grid cells (1° × 1°) where dust aerosols (DA) were detected over South Middle East by the satellite algorithm (left axis) and the percent coverage of the region by dusty grid cells (right axis). The error bars represent the year-by-year variability by means of computed 2005–2019 standard deviations. (**b**) Inter-annual variability and linear trend of the relative frequency of dust aerosols (DA) over South Middle East.

4. Conclusions

A satellite algorithm was used for detecting dust aerosols (DA) and building a climatology of the frequency of occurrence of DA for the 15-year period 2005–2019. The algorithm uses daily information of MODIS-Aqua based aerosol optical depth (AOD) and Ångström exponent (a) and OMI-Aura based Aerosol Index (AI). Applying specific thresholds to these aerosol properties, the algorithm detects coarse and absorbing dust aerosols over grid cells at 1° × 1° latitude–longitude resolution all over the globe. After its operation on a daily basis over the period of 2005–2019, the algorithm computed the frequency of occurrence of DA on a mean monthly and annual basis. In addition, 15-year average frequencies of DA as well as regional averages for specific world areas of interest (great deserts and downwind regions) were calculated. Finally, the inter-annual variability of DA over the globe and the selected study regions was studied, emphasizing the observed possible trends.

- The greatest frequencies of occurrence of dust (40–165 days/year) were observed over the North Hemisphere, across the Global Dust Belt (GDB) extending from the western coast of North Africa to China, including the regions of Middle East and Central and Southern Asia. GDB includes the greatest world deserts, namely the Sahara, Middle East, Arabian, Taklamakan and Gobi, from which dust aerosols are transported to remote regions such as the Tropical Atlantic Ocean and the Mediterranean Basin. The maximum frequencies (165 days/year) were observed over the western part of the Sahara and the broader Bodélé area, whereas very high frequencies were observed over the Taklamakan (140 days/year) and Gobi (110 days/year) deserts in Asia. High frequencies of DA (80 days/year) were also observed over the northern part of Middle East as well as over the eastern part of Sahara. Over all these areas, dust aerosols were encountered in more than 50% of the days for which the satellite algorithm operated.
- A notable seasonal and inter-annual variability of dust aerosols was revealed by the results of the satellite algorithm. In general, the strongest frequency of occurrence on a global basis was observed in boreal summer, and more specifically in June, when dust aerosols were detected in more than 10 days/month over extended desert areas, namely the Sahara, Middle East and Asian deserts. During June, dust aerosols cover about 3.6% of the global areas for which the algorithm operated (i.e., 633,463 grid cells). On the other hand, the minimum frequencies of DA were observed in boreal winter, and more specifically in November, when dust was observed over desert areas only on a few days (mainly up to 2 or 3 days/month). This seasonal variability of DA on a global basis slightly differs from one region to another. Thus, DA frequencies are maximum in spring (mainly late) over East Sahara, Taklamakan, Gobi, Thar and North Middle East deserts, and in (mainly early) summer over West Sahara, Tropical Atlantic Ocean and the South Middle East desert. Double maximum frequencies, primarily in summer and secondary in spring were are observed over the Mediterranean basin.
- The frequency of DA changes year by year, even on a global scale. Thus, during the 15-year study period, the lowest frequency of global DA was observed in 2007 (0.0143) and 2009 (0.0146) and the highest one (0.0290) in 2018. During the period of 2005–2019, the global dust frequency fluctuated, showing an increased trend equal to 56.2%, which is not statistically significant according to the applied Mann–Kendal test but marginally significant according to the slope error. Increasing trends of the frequency of occurrence of dust were observed for all the selected study regions, except for the North Middle East, where decreasing trend was noted. The strongest increase, equal to 92% (statistically significant according to the applied Mann–Kendal test) was observed over the West Tropical Atlantic Ocean. According to the applied Mann–Kendall test, the statistically significant trends are those calculated for the Globe, East Sahara, West Sahara, Mediterranean, Taklamakan and West Tropical Atlantic Ocean. However, when the statistical significance is ascertained from the computed standard error of the slope of the applied linear regression, three (3) other regions were found to have undergone significant trends, namely East Tropical Atlantic Ocean, South Middle East and Gulf of Guinea. Such inter-annual trends of the frequency of occurrence of global or regional dust may have significant implications in various aspects ranging from climate to health and ocean biogeochemistry.
- The seasonal and inter-annual variability of the presence of dust is connected to dust sources' activation (e.g., desertification) and/or to dust removal and deposition mechanisms (e.g., changes in precipitation). Years with low precipitation are associated with strong dust presence in the atmosphere due to the reduced wet deposition [124]. Thus, for example, the strong increase in DA over the West Tropical Atlantic Ocean, compared to the slighter increase over the East Tropical Atlantic Ocean, given that both regions undergo transport of dust from Sahara, can be attributed to (weakened) deposition.
- The present algorithm has limitations, since it uses columnar aerosol products. Thus, in cases where coarse strongly scattering sea-salt aerosols in the oceanic boundary

layer coexist with overlying (in the free troposphere) fine and strongly absorbing carbonaceous aerosols, the algorithm misidentifies the predominant aerosol type in the atmospheric column as dust (coarse moderately absorbing). This is the case in southeast Atlantic Ocean, off the coasts of Angola, where biomass burning aerosols from the African mainland are exported westwards, into the ocean, from July to September and overlie the marine boundary layer sea-salt aerosols.

In the future, the results of the present study will be compared to similar results obtained with the same algorithm using different satellite data, such as MISR (Multi-angle Imaging SpectroRadiometer). In addition, the current algorithm, using columnar satellite data, can be improved by using contemporary, but spatially and temporally limited as of now, vertically resolved satellite products (for example CALIOP-CALIPSO data) or climatological 3-D aerosol climatologies (MERRA-2), thus providing more accurate results as well as information about the altitude and layers of dust aerosols.

Supplementary Materials: The following are available online at https://www.mdpi.com/2072-4292/13/3/359/s1, Figure S1: Global distribution of the annual absolute frequency of occurrence of dust aerosols (in number of days/year) for Ångström Exponent computed at 470 nm–660 nm over land and 470 nm–2130 nm over ocean (a), at 470 nm–660 nm over land and 470 nm–650 nm over ocean (b) and 550 nm–660 nm over land and 550 nm–650 nm over ocean (c). The results are for the year 2005, Figure S2: Global distribution of the annual absolute frequency of occurrence of dust aerosols (in number of days/year) for AI thresholds equal to 0.8 (a) and 1.2 (b). The results are for the year 2005, Figure S3: Global distribution of the monthly absolute frequency of occurrence of dust aerosols (in number of days/month) for AI thresholds equal to 0.8 (left column) and 1.2 (right column). Each row corresponds to the months of the year, from January (top) to December (bottom). The results are for the year 2005, Figure S4: Global distribution of the annual absolute frequency of occurrence of dust aerosols (in number of days/year) for a threshold of Ångström Exponent equal to 0.4 (a) and 0.7 (b). The results are for the year 2005, Figure S5: Global distribution of the monthly absolute frequency of occurrence of dust aerosols (in number of days/year) for a threshold of Ångström Exponent equal to 0.4 (left) and 0.7 (right). The results are for the year 2005, Figure S6: Global distribution of the MERRA-2 based monthly vertical distribution of extinction coefficients (in Km^{-1}) of sulfate (orange curves), dust (yellow curves), sea-salt (blue curves), black carbon (indigo curves) and organic carbon (red curves) aerosols over the southeast Atlantic Ocean (5°E–14°E and (17°S–6°S). Total aerosol extinction coefficients (black curves) are also shown in each plot. Each row corresponds to the months of the year, from January (i, top) to December (xii, bottom). The results are averaged over the period 2005–2019, Figure S7: Intra-annual variability, for each year of the period 2005–2019, of the absolute frequency of occurrence of dust aerosols (DA) over the $1^\circ \times 1^\circ$ grid cells of each selected world region. Results are given for: (i) the entire globe, (ii) East Sahara, (iii) West Sahara, (iv) East Tropical Atlantic, (v) West Tropical Atlantic, (vi) Gulf of Guinea, (vii) Taklamakan, (viii) Gobi, (ix) Mediterranean, (x) North Middle East and South Middle East refer to the overall number of grid cells (counts) over which DA have been detected by the satellite algorithm during each year.

Author Contributions: Conceptualization, N.H. and A.G.; methodology, N.H. and A.G.; software, N.H., A.G. and M.G.; formal analysis, M.G.; investigation, N.H., and M.G.; resources, N.H., M.G., A.G. and M.-B.K.-C.; data curation, N.H., M.G. and M.-B.K.-C.; writing—original draft preparation, M.G.; writing—review and editing, N.H., A.G., N.M., M.-B.K.-C. and M.G.; visualization, M.G.; supervision, N.H.; project administration, N.H.; funding acquisition, N.H. and N.M. All authors have read and agreed to the published version of the manuscript.

Funding: This research received no external funding.

Institutional Review Board Statement: Not applicable.

Informed Consent Statement: Not applicable.

Data Availability Statement: Publicly available datasets were analyzed in this study. This data can be found here: [https://ladsweb.modaps.eosdis.nasa.gov/search/].

Acknowledgments: We acknowledge support by the project "PANhellenic infrastructure for Atmospheric Composition and climatE change" (MIS 5021516) which is implemented under the Action "Reinforcement of the Research and Innovation Infrastructure", funded by the Operational Programme "Competitiveness, Entrepreneurship and Innovation" (NSRF 2014–2020) and co-financed by Greece and the European Union (European Regional Development Fund).

Conflicts of Interest: The authors declare no conflict of interest.

References

1. Jaenicke, R. Aerosol physics and chemistry. In *Landolt-Börnstein Numerical Data and Functional Relationship in Science and Technology, New Series Group V, Geophysics and Space Research, Meteorology*; Springer: Heidelberg, Germany, 1988; Volume 4, pp. 391–457.
2. Ramanathan, V.; Crutzen, P.J.; Kiehl, J.T.; Rosenfeld, D. Aerosols, Climate, and the Hydrological Cycle. *Science* **2001**, *294*, 2119–2124. [CrossRef] [PubMed]
3. Heald, C.L.; Ridley, D.A.; Kroll, J.H.; Barrett, S.R.H.; Cadypereira, K.E.; Alvarado, M.J.; Holmes, C.D. Contrasting the direct radiative effect and direct radiative forcing of aerosols. *Atmos. Chem. Phys.* **2014**, *14*, 5513–5527. [CrossRef]
4. Prospero, J.; Ginoux, P.; Torres, O.; Nicholson, S.; Gill, T. Environmental characterization of global sources of atmospheric soil dust identified with the NIMBUS 7 Total Ozone Mapping Sectrometer (TOMS) absorbing aerosol product. *Rev. Geophys.* **2002**, *40*, 2-1–2-31. [CrossRef]
5. Washington, R.W.; Todd, M.C.; Middleton, N.; Goudie, A.S. Dust-storm source areas determined by the total ozone moni-toring spectrometer and surface observations. *Ann. Assoc. Am. Geogr.* **2003**, *93*, 297–313. [CrossRef]
6. Tegen, I.; Werner, M.; Harrison, S.P.; Kohfeld, K.E. Relative importance of climate and land use in determining present and future global soil dust emission. *Geophys. Res. Lett.* **2004**, *31*, L05105. [CrossRef]
7. Bullard, J.E.; Baddock, M.C.; Bradwell, T.; Crusius, J.; Darlington, E.F.; Gaiero, D.; Gassó, S.; Gisladottir, G.; Hodgkins, R.; McCulloch, R.; et al. High-latitude dust in the Earth system. *Rev. Geophys.* **2016**, *54*, 447–485. [CrossRef]
8. Velasco-Merino, C.; Mateos, D.; Toledano, C.; Prospero, J.M.; Molinie, J.; Euphrasie-Clotilde, L.; González, R.; Cachorro, V.E.; Calle, A.; De Frutos, A.M. Impact of long-range transport over the Atlantic Ocean on Saharan dust optical and microphysical properties based on AERONET data. *Atmos. Chem. Phys.* **2018**, *18*, 9411–9424. [CrossRef]
9. Barkan, J.; Alpert, P. Synoptic analysis of a rare event of Saharan dust reaching the Arctic region. *Weather* **2010**, *65*, 208–211. [CrossRef]
10. Vincent, R. The Effect of Arctic Dust on the Retrieval of Satellite Derived Sea and Ice Surface Temperatures. *Sci. Rep.* **2018**, *8*, 9727. [CrossRef]
11. Tanre, D.; Kaufman, Y.J.; Holben, B.N.; Chatenet, B.; Karnieli, A.; Lavenu, F.; Blarel, L.; Dubovik, O.; Remer, L.A.; Smirnov, A. Climatology of dust aerosol size distribution and optical properties derived from remotely sensed data in the solar spectrum. *J. Geophys. Res. Atmos.* **2001**, *106*, 18205–18217. [CrossRef]
12. Fan, J.; Wang, Y.; Rosenfeld, D.; Liu, X. Review of Aerosol–Cloud Interactions: Mechanisms, Significance, and Challenges. *J. Atmos. Sci.* **2016**, *73*, 4221–4252. [CrossRef]
13. Li, Z.; Lau, W.K.M.; Ramanathan, V.; Wu, G.; Ding, Y.; Manoj, M.G. Aerosol and monsoon climate interactions over Asia. *Rev. Geophys.* **2016**, *54*, 866–929. [CrossRef]
14. Li, X.; Zhang, Q.; Xue, H. The role of initial cloud condensation nuclei concentration in hail using the WRF NSSL 2-moment microphysics scheme. *Adv. Atmos. Sci.* **2017**, *34*, 1106–1120. [CrossRef]
15. Jiang, J.H.; Su, H.; Huang, L.; Wang, Y.; Massie, S.; Zhao, B.; Omar, A.H.; Wang, Z. Contrasting effects on deep convective clouds by different types of aerosols. *Nat. Commun.* **2018**, *9*, 1–7. [CrossRef] [PubMed]
16. Lu, Z.; Liu, X.; Zhang, Z.; Zhao, C.; Meyer, K.; Rajapakshe, C.; Wu, C.; Yang, Z.; Penner, J.E. Biomass smoke from southern Africa can significantly enhance the brightness of stratocumulus over the southeastern Atlantic Ocean. *Proc. Natl. Acad. Sci. USA* **2018**, *115*, 2924–2929. [CrossRef] [PubMed]
17. Chen, Q.; Yin, Y.; Jiang, H.; Chu, Z.; Xue, L.; Shi, R.; Zhang, X.; Chen, J. The Roles of Mineral Dust as Cloud Condensation Nuclei and Ice Nuclei during the Evolution of a Hail Storm. *J. Geophys. Res. Atmos.* **2019**, *124*, 14262–14284. [CrossRef]
18. Rosenfeld, D.; Zhu, Y.; Wang, M.; Zhengi, D.Y.; Goren, T.; Yu, S. Aerosol-driven droplet concentrations dominate coverage and water of oceanic low-level clouds. *Science* **2019**, *363*, eaav0566. [CrossRef] [PubMed]
19. Rosenfeld, D.; Rudich, Y.; Lahav, R. Desert dust suppressing precipitation: A possible desertification feedback loop. *Proc. Natl. Acad. Sci. USA* **2001**, *98*, 5975–5980. [CrossRef]
20. Dagan, G.; Koren, I.; Altaratz, O. Competition between core and periphery-based processes in warm convective clouds—From invigoration to suppression. *Atmos. Chem. Phys.* **2015**, *15*, 2749–2760. [CrossRef]
21. Guo, J.; Deng, M.; Lee, S.S.; Wang, F.; Li, Z.; Zhai, P.; Liu, H.; Lv, W.; Yao, W.; Li, X. Delaying precipitation and lightning by air pollution over the Pearl River Delta. Part I: Observational analyses. *J. Geophys. Res. Atmos.* **2016**, *121*, 6472–6488. [CrossRef]
22. Lee, S.; Kim, B.-G.; Yum, S.S.; Seo, K.-H.; Jung, C.-H.; Um, S.J. Effects of aerosol on evaporation, freezing and precipitation in a multiple cloud system. *Clim. Dyn.* **2016**, *48*, 1069–1087. [CrossRef]
23. Liu, H.; Guo, J.; Koren, I.; Altaratz, O.; Dagan, G.; Wang, Y.; Jiang, J.H.; Zhai, P.; Yung, Y.L. Non-Monotonic Aerosol Effect on Precipitation in Convective Clouds over Tropical Oceans. *Sci. Rep.* **2019**, *9*, 7809. [CrossRef] [PubMed]

24. Jiang, H.; Feingold, G.; Koren, I. Effect of aerosol on trade cumulus cloud morphology. *J. Geophys. Res. Atmos.* **2009**, *114*, 11209. [CrossRef]
25. Saleeby, S.M.; Berg, W.; Heever, S.C.V.D.; L'Ecuyer, T.S. Impact of Cloud-Nucleating Aerosols in Cloud-Resolving Model Simulations of Warm-Rain Precipitation in the East China Sea. *J. Atmos. Sci.* **2010**, *67*, 3916–3930. [CrossRef]
26. Dagan, G.; Koren, I.; Altaratz, O. Aerosol effects on the timing of warm rain processes. *Geophys. Res. Lett.* **2015**, *42*, 4590–4598. [CrossRef]
27. Rosenfeld, D.; Lohmann, U.; Raga, G.B.; O'Dowd, C.D.; Kulmala, M.; Fuzzi, S.; Reissell, A.; Andreae, M.O. Flood or Drought: How Do Aerosols Affect Precipitation? *Science* **2008**, *321*, 1309–1313. [CrossRef]
28. Noppel, H.; Blahak, U.; Seifert, A.; Beheng, K.D. Simulations of a hailstorm and the impact of CCN using an advanced two-moment cloud microphysical scheme. *Atmos. Res.* **2010**, *96*, 286–301. [CrossRef]
29. Xue, L.; Teller, A.; Rasmussen, R.; Geresdi, I.; Pan, Z.; Liu, X. Effects of Aerosol Solubility and Regeneration on Mixed-Phase Orographic Clouds and Precipitation. *J. Atmos. Sci.* **2012**, *69*, 1994–2010. [CrossRef]
30. Fan, J.; Leung, L.R.; Rosenfeld, D.; Chen, Q.; Li, Z.; Zhang, J.; Yan, H. Microphysical effects determine macrophysical response for aerosol impacts on deep convective clouds. *Proc. Natl. Acad. Sci. USA* **2013**, *110*, E4581–E4590. [CrossRef] [PubMed]
31. Falkowski, P.G.; Barber, R.T.; Smetacek, V. Biogeochemical Controls and Feedbacks on Ocean Primary Production. *Science* **1998**, *281*, 200–206. [CrossRef]
32. Fung, I.Y.; Meyn, S.K.; Tegen, I.; Doney, S.C.; John, J.G.; Bishop, J.K.B. Iron supply and demand in the upper ocean. *Glob. Biogeochem. Cycles* **2000**, *14*, 281–295. [CrossRef]
33. Jickells, T.D.; Anderson, K.; Andersen, K.K.; Baker, A.R.; Bergametti, G.; Brooks, N.; Cao, J.J.; Boyd, P.W.; Duce, R.A.; Hunter, K.A.; et al. Global Iron Connections between Desert Dust, Ocean Biogeochemistry, and Climate. *Science* **2005**, *308*, 67–71. [CrossRef] [PubMed]
34. Pérez, C.; Nickovic, S.; Pejanovic, G.; Baldasano, J.M.; Özsoy, E.; García-Pando, C.P. Interactive dust-radiation modeling: A step to improve weather forecasts. *J. Geophys. Res. Atmos.* **2006**, *111*. [CrossRef]
35. Gkikas, A.; Obiso, V.; García-Pando, C.P.; Jorba, O.; Hatzianastassiou, N.; Vendrell, L.; Basart, S.; Solomos, S.; Gassó, S.; Baldasano, J.M. Direct radiative effects during intense Mediterranean desert dust outbreaks. *Atmos. Chem. Phys.* **2018**, *18*, 8757–8787. [CrossRef]
36. Gkikas, A.; Giannaros, T.; Kotroni, V.; Lagouvardos, K. Assessing the radiative impacts of an 1233 extreme desert dust outbreak and the potential improvements on short-term weather forecasts: The case of February. *Atmos. Res.* **2019**, *226*, 152–170. [CrossRef]
37. De Longueville, F.; Hountondji, Y.C.; Henry, S.; Ozer, P. What do we know about effects of desert dust on air quality and human health in West Africa compared to other regions? *Sci. Total Environ.* **2010**, *409*, 1–8. [CrossRef]
38. Mahowald, N.; Kloster, S.; Engelstaedter, S.; Moore, J.K.; Mukhopadhyay, S.; McConnell, J.R.; Albani, S.; Doney, S.C.; Bhattacharya, A.; Curran, M.A.J.; et al. Observed 20th century desert dust variability: Impact on climate and biogeochemistry. *Atmos. Chem. Phys.* **2010**, *10*, 10875–10893. [CrossRef]
39. Shao, Y.; Wyrwoll, K.-H.; Chappell, A.; Huang, J.; Lin, Z.; McTainsh, G.; Mikami, M.; Tanaka, T.Y.; Wang, X.; Yoon, S. Dust cycle: An emerging core theme in Earth system science. *Aeolian Res.* **2011**, *2*, 181–204. [CrossRef]
40. Giannadaki, D.; Pozzer, A.; Lelieveld, J. Modeled global effects of airborne desert dust on air quality and premature mortality. *Atmos. Chem. Phys.* **2014**, *14*, 957–968. [CrossRef]
41. Koren, I.; Kaufman, Y.J.; Washington, R.; Todd, M.C.; Rudich, Y.; Martins, J.V.; Rosenfeld, D. The Bodélé depression: A single spot in the Sahara that provides most of the mineral dust to the Amazon forest. *Environ. Res. Lett.* **2006**, *1*, 014005. [CrossRef]
42. Gkikas, A.; Basart, S.; Hatzianastassiou, N.; Marinou, E.; Amiridis, V.; Kazadzis, S.; Pey, J.; Querol, X.; Jorba, O.; Gassó, S.; et al. Mediterranean intense desert dust outbreaks and their vertical structure based on remote sensing data. *Atmos. Chem. Phys.* **2016**, *16*, 8609–8642. [CrossRef]
43. Proestakis, E.; Amiridis, V.; Marinou, E.; Georgoulias, A.K.; Solomos, S.; Kazadzis, S.; Chimot, J.; Che, H.; Alexandri, G.; Binietoglou, I.; et al. Nine-year spatial and temporal evolution of desert dust aerosols over South and East Asia as revealed by CALIOP. *Atmos. Chem. Phys.* **2018**, *18*, 1337–1362. [CrossRef]
44. Koven, C.D.; Fung, I. Identifying global dust source areas using high-resolution land surface form. *J. Geophys. Res. Atmos.* **2008**, *113*. [CrossRef]
45. Ridley, D.A.; Heald, C.L.; Kok, J.; Zhao, C. An observationally constrained estimate of global dust aerosol optical depth. *Atmos. Chem. Phys.* **2016**, *16*, 15097–15117. [CrossRef]
46. Hatzianastassiou, N.; Wobrock, W.; Flossmann, A.I. The effect of cloud-processing of aerosol particles on clouds and radiation. *Tellus B Chem. Phys. Meteorol.* **1998**, *50*, 478–490. [CrossRef]
47. Boucher, O.; Randall, D.; Artaxo, P.; Bretherton, C.; Feingold, G.; Forster, P.; Kerminen, V.-M.; Kondo, Y.; Liao, H.; Lohmann, U.; et al. Clouds and Aerosols. In *Climate Change 2013: The Physical Science Basis. Contribution of Working Group I to the Fifth Assessment Report of the Intergovernmental Panel on Climate Change*; Stocker, T.F., Qin, D., Plattner, G.-K., Tignor, M., Allen, S.K., Boschung, J., Nauels, A., Xia, Y., Bex, V., Midgley, P.M., Eds.; Cambridge University Press: Cambridge, UK; New York, NY, USA, 2013.
48. Wang, W.; Sheng, L.; Dong, X.; Qu, W.; Sun, J.; Jin, H.; Logan, T. Dust aerosol impact on the retrieval of cloud top height from satellite observations of CALIPSO, CloudSat and MODIS. *J. Quant. Spectrosc. Radiat. Transf.* **2017**, *188*, 132–141. [CrossRef]
49. Middleton, N.J. *Desertification and Wind Erosion in the Western Sahel: The Example of Mauritania*; Research Paper 40; School of Geography, University of Oxford: Oxford, UK, 1987.

50. Alibekov, L.; Alibekov, D. Causes and Socio-Economic Consequences of Desertification in Central Asia. In *The Socio-Economic Causes and Consequences of Desertification in Central Asia. NATO Science for Peace and Security Series (Series C: Environmental Security)*; Behnke, R., Ed.; Springer: Dordrecht, The Netherlands, 2008. [CrossRef]
51. Vickery, K.J.; Eckardt, F.D.; Bryant, R.G. A sub-basin scale dust plume source frequency inventory for southern Africa, 2005–2008. *Geophys. Res. Lett.* **2013**, *40*, 5274–5279. [CrossRef]
52. Washington, R.; Todd, M.C. Atmospheric controls on mineral dust emission from the Bodélé Depression, Chad: The role of the low level jet. *Geophys. Res. Lett.* **2005**, *32*. [CrossRef]
53. Wang, X.; Liu, J.; Che, H.; Ji, F.; Liu, J. Spatial and temporal evolution of natural and anthropogenic dust events over northern China. *Sci. Rep.* **2018**, *8*, 2141. [CrossRef]
54. Ginoux, P.; Prospero, J.M.; Gill, T.E.; Hsu, N.C.; Zhao, M. Global-scale attribution of anthropogenic and natural dust sources and their emission rates based on MODIS Deep Blue aerosol products. *Rev. Geophys.* **2012**, *50*, 305. [CrossRef]
55. Afeti, G.M.; Resch, F.J. Physical characteristics of Saharan dust near the Gulf of Guinea. *Atmos. Environ.* **2000**, *34*, 1273–1279. [CrossRef]
56. Bibi, M.; Saad, M.; Masmoudi, M.; Laurent, B.; Alfaro, S.C. Long-term (1980–2018) spatial and temporal variability of the atmospheric dust load and deposition fluxes along the North-African coast of the Mediterranean Sea. *Atmos. Res.* **2020**, *234*, 104689. [CrossRef]
57. Goudie, A.S.; Middleton, N.J. The changing frequency of dust storms through time. *Clim. Chang.* **1992**, *20*, 197–225. [CrossRef]
58. Engelstaedter, S.; Tegen, I.; Washington, R. North African dust emissions and transport. *Earth Sci. Rev.* **2006**, *79*, 73–100. [CrossRef]
59. Yu, Y.; Kalashnikova, O.V.; Garay, M.J.; Notaro, M. Climatology of Asian dust activation and transport potential based on MISR satellite observations and trajectory analysis. *Atmos. Chem. Phys.* **2019**, *19*, 363–378. [CrossRef]
60. Levy, R.C.; Mattoo, S.; Munchak, L.A.; Remer, L.A.; Sayer, A.M.; Patadia, F.; Hsu, N.C. The Collection 6 MODIS aerosol products over land and ocean. *Atmos. Meas. Tech.* **2013**, *6*, 2989–3034. [CrossRef]
61. Bilal, M.; Nazeer, M.; Shengqiang, W.; Ding, X.; Wei, J. Global Validation of MODIS C6 and C6.1 Merged Aerosol Products over Diverse Vegetated Surfaces. *Remote Sens.* **2018**, *10*, 475. [CrossRef]
62. Tian, X.; Liu, Q.; Li, X.; Wei, J. Validation and Comparison of MODIS C6.1 and C6 Aerosol Products over Beijing, China. *Remote Sens.* **2018**, *10*, 2021. [CrossRef]
63. Huang, Y.; Zhu, B.; Zhu, Z.; Zhang, T.; Gong, W.; Ji, Y.; Xia, X.; Wang, L.; Zhou, X.; Chen, D. Evaluation and Comparison of MODIS Collection 6.1 and Collection 6 Dark Target Aerosol Optical Depth over Mainland China under Various Conditions Including Spatiotemporal Distribution, Haze Effects, and Underlying Surface. *Earth Space Sci.* **2019**, *6*, 2575–2592. [CrossRef]
64. Wei, J.; Li, Z.; Peng, Y.; Sun, L. MODIS Collection 6.1 aerosol optical depth products over land and ocean: Validation and comparison. *Atmos. Environ.* **2019**, *201*, 428–440. [CrossRef]
65. Torres, O.; Ahn, C.; Chen, Z. Improvements to the OMI near-UV aerosol algorithm using A-train CALIOP and AIRS observations. *Atmos. Meas. Tech.* **2013**, *6*, 3257–3270. [CrossRef]
66. Remer, L.A.; Mattoo, S.K.; Levy, R.C.; Munchak, L.A. MODIS 3 km aerosol product: Algorithm and global perspective. *Atmos. Meas. Tech.* **2013**, *6*, 1829–1844. [CrossRef]
67. Gupta, P.; Remer, L.A.; Patadia, F.; Levy, R.C.; Christopher, S.A. High-Resolution Gridded Level 3 Aerosol Optical Depth Data from MODIS. *Remote Sens.* **2020**, *12*, 2847. [CrossRef]
68. Ginoux, P.; Garbuzov, D.; Hsu, N.C. Identification of anthropogenic and natural dust sources using Moderate Resolution Imaging Spectroradiometer (MODIS) Deep Blue level 2 data. *J. Geophys. Res. Atmos.* **2010**, *115*, 05204. [CrossRef]
69. Herman, J.R.; Bhartia, P.K.; Torres, O.; Hsu, N.C.; Seftor, C.J.; Celarier, E. Global distribution of UV-absorbing aerosols from Nimbus-7/ TOMS data. *J. Geophys. Res.* **1997**, *102*, 16911–16923. [CrossRef]
70. Torres, O.; Bhartia, P.K.; Herman, J.R.; Ahmad, Z.; Gleason, J. Derivation of aerosol properties from satellite measurements of backscattered ultraviolet radiation: Theoretical basis. *J. Geophys. Res. Atmos.* **1998**, *103*, 17099–17110. [CrossRef]
71. Takemura, T.; Nakajima, T.; Dubovik, O.; Holben, B.N.; Kinne, S. Single-Scattering Albedo and Radiative Forcing of Various Aerosol Species with a Global Three-Dimensional Model. *J. Clim.* **2002**, *15*, 333–352. [CrossRef]
72. Pace, G.; Di Sarra, A.; Meloni, D.; Piacentino, S.; Chamard, P. Aerosol optical properties at Lampedusa (Central Mediterranean). Influence of transport and identification of different aerosol types. *Atmos. Chem. Phys.* **2006**, *6*, 697–713. [CrossRef]
73. Tolédano, C.; Wiegner, M.; Garhammer, M.; Seefeldner, M.; Gasteiger, J.; Muller, D.; Koepke, P. Spectral aerosol optical depth characterization of desert dust during SAMUM 2006. *Tellus B Chem. Phys. Meteorol.* **2009**, *61*, 216–228. [CrossRef]
74. Gkikas, A.; Hatzianastassiou, N.; Mihalopoulos, N.; Katsoulis, V.; Kazadzis, S.; Pey, J.; Querol, X.; Torres, O. The regime of intense desert dust episodes in the Mediterranean based on contemporary satellite observations and ground measurements. *Atmos. Chem. Phys.* **2013**, *13*, 12135–12154. [CrossRef]
75. Huneeus, N.; Schulz, M.; Balkanski, Y.; Griesfeller, J.; Prospero, J.M.; Kinne, S.; Bauer, S.; Boucher, O.; Chin, M.; Dentener, F.; et al. Global dust model intercomparison in AeroCom phase I. *Atmos. Chem. Phys.* **2011**, *11*, 7781–7816. [CrossRef]
76. Yuan, C.; Lau, W.K.M.; Li, Z.; Cribb, M.C. Relationship between Asian monsoon strength and transport of surface aerosols to the Asian Tropopause Aerosol Layer (ATAL): Interannual variability and decadal changes. *Atmos. Chem. Phys.* **2019**, *19*, 1901–1913. [CrossRef]
77. Chiapello, I.; Moulin, C. TOMS and METEOSAT satellite records of the variability of Saharan dust transport over the Atlantic during the last two decades (1979–1997). *Geophys. Res. Lett.* **2002**, *29*, 17-1–17-4. [CrossRef]

78. Evan, A.T.; Mukhopadhyay, S. Optical depth of Atlantic dust as NetCDF files. *PANGAEA* **2010**. Supplement to: Evan, A.T.; Mukhopadhyay, S. African dust over the Northern Tropical Atlantic: 1955–2008. *J. Appl. Meteorol. Climatol.* **2010**, *49*, 2213–2229, doi:10.1175/2010JAMC2485.1. [CrossRef]
79. Wang, K.; Liu, C.; Wan, K.-Y. Transport of the Saharan dust air plumes over the tropical North Atlantic from FORMOSAT–3/COSMIC observation. *Atmos. Pollut. Res.* **2014**, *5*, 539–553. [CrossRef]
80. D'Almeida, G.A. Desert aerosol: Characteristics and effects on climate. In *Paleoclimatology and Paleometeorology: Modern and Past Patterns of Global Atmospheric Transport*; Leinen, M., Sarnthein, M., Eds.; Kluwer Academic Publishers: Dordrecht, The Netherlands, 1989; pp. 311–338.
81. Barnaba, F.; Gobbi, G.P. Modeling the Aerosol Extinction versus Backscatter Relationship for Lidar Applications: Maritime and Continental Conditions. *J. Atmos. Ocean. Technol.* **2004**, *21*, 428–442. [CrossRef]
82. Engelstaedter, S.; Washington, R. Temporal controls on global dust emissions: The role of surface gustiness. *Geophys. Res. Lett.* **2007**, *34*. [CrossRef]
83. Haywood, J.M.; Pelon, J.; Formenti, P.; Bharmal, N.; Brooks, M.; Capes, G.; Chazette, P.; Chou, C.; Christopher, S.; Coe, H.; et al. Overview of the Dust and Biomass-burning Experiment and African Monsoon Multidisciplinary Analysis Special Observing Period-0. *J. Geophys. Res. Atmos.* **2008**, *113*. [CrossRef]
84. Marticorena, B.; Chatenet, B.; Rajot, J.L.; Traoré, S.; Coulibaly, M.; Diallo, A.; Koné, I.; Maman, A.; Ndiaye, T.; Zakou, A. Temporal variability of mineral dust concentrations over West Africa: Analyses of a pluriannual monitoring from the AMMA Sahelian Dust Transect. *Atmos. Chem. Phys.* **2010**, *10*, 8899–8915. [CrossRef]
85. Huang, J.; Minnis, P.; Yan, H.; Yi, Y.; Chen, B.; Zhang, L.; Ayers, J.K. Dust aerosol effect on semi-arid climate over Northwest China detected from A-Train satellite measurements. *Atmos. Chem. Phys.* **2010**, *10*, 6863–6872. [CrossRef]
86. Ashpole, I.; Washington, R. A new high-resolution central Saharan dust source map from automated satellite dust plume tracking. *J. Geophys. Res.* **2013**, *118*, 6981–6995. [CrossRef]
87. Balarabe, M.; Abdullah, K.; Nawawi, M.N.M. Long-Term Trend and Seasonal Variability of Horizontal Visibility in Nigerian Troposphere. *Atmosphere* **2015**, *6*, 1462–1486. [CrossRef]
88. Aklesso, M.; Kumar, K.R.; Bu, L.; Boiyo, R. Analysis of spatial-temporal heterogeneity in remotely sensed aerosol properties observed during 2005–2015 over three countries along the Gulf of Guinea Coast in Southern West Africa. *Atmos. Environ.* **2018**, *182*, 313–324. [CrossRef]
89. Liu, X.; Yin, Z.-Y. Sensitivity of East Asian monsoon climate to the uplift of the Tibetan Plateau. *Palaeogeogr. Palaeoclim. Palaeoecol.* **2002**, *183*, 223–245. [CrossRef]
90. Huang, J.; Minnis, P.; Chen, B.; Huang, Z.; Liu, Z.; Zhao, Q.; Yi, Y.; Ayers, J.K. Long-range transport and vertical structure of Asian dust from CALIPSO and surface measurements during PACDEX. *J. Geophys. Res. Atmos.* **2008**, *113*. [CrossRef]
91. Liu, Z.; Liu, D.; Huang, J.; Vaughan, M.; Uno, I.; Sugimoto, N.; Kittaka, C.; Trepte, C.; Wang, Z.; Hostetler, C.; et al. Airborne dust distributions over the Tibetan Plateau and surrounding areas derived from the first year of CALIPSO lidar observations. *Atmos. Chem. Phys.* **2008**, *8*, 5045–5060. [CrossRef]
92. Lin, C.; Guang-Yu, S.; Ling-Zhi, Z.; Sai-Chun, T. Assessment of Dust Aerosol Optical Depth and Shortwave Radiative Forcing over the Northwest Pacific Ocean in Spring Based on Satellite Observations. *Atmos. Ocean. Sci. Lett.* **2009**, *2*, 224–229. [CrossRef]
93. Creamean, J.; Spackman, J.R.; Davis, S.M.; White, A.B. Climatology of long-range transported Asian dust along the West Coast of the United States. *J. Geophys. Res. Atmos.* **2014**, *119*. [CrossRef]
94. Yoon, J.-E.; Lim, J.-H.; Shim, J.-M.; Kwon, J.-I.; Kim, I.-N. Spring 2018 Asian Dust Events: Sources, Transportation, and Potential Biogeochemical Implications. *Atmosphere* **2019**, *10*, 276. [CrossRef]
95. Jethva, H.; Satheesh, S.K.; Srinivasan, J. Seasonal variability of aerosols over the Indo-Gangetic basin. *J. Geophys. Res. Atmos.* **2005**, *110*. [CrossRef]
96. Ramaswamy, V.; Muraleedharan, P.M.; Babu, C.P. Mid-troposphere transport of Middle-East dust over the Arabian Sea and its effect on rainwater composition and sensitive ecosystems over India. *Sci. Rep.* **2017**, *7*, 1–8. [CrossRef] [PubMed]
97. Kumar, K.R.; Attadaa, R.; Prasad, H.; Dasari, H.P.; Vellorec, R.K.; Langodana, S.; Abualnajaa, Y.O.; Hoteita, I. Aerosol Optical Depth variability over the Arabian Peninsula as inferred from satellite measurements. *Atmos. Environ.* **2018**, *187*, 346–357. [CrossRef]
98. Prospero, J.M.; Nees, R.T. Impact of the North African drought and El Niño on mineral dust in the Barbados trade winds. *Nat. Cell Biol.* **1986**, *320*, 735–738. [CrossRef]
99. Hatzianastassiou, N.; Kalaitzi, N.; Gavrouzou, M.; Gkikas, A.; Korras-Carraca, M.B.; Mihalopoulos, N. A Climatological Satellite Assessment of Absorbing Carbonaceous Aerosols on a Global Scale. *Atmosphere* **2019**, *10*, 671. [CrossRef]
100. Zuidema, P.; Redemann, J.; Haywood, J.M.; Wood, R.; Piketh, S.; Hipondoka, M.; Formenti, P. Smoke and Clouds above the Southeast Atlantic: Upcoming Field Campaigns Probe Absorbing Aerosol's Impact on Climate. *Bull. Am. Meteorol. Soc.* **2016**, *97*, 1131–1135. [CrossRef]
101. Gelaro, R.; Mccarty, W.; Suárez, M.J.; Todling, R.; Molod, A.; Takacs, L.; Randles, C.A.; Darmenov, A.; Bosilovich, M.G.; Reichle, R.H.; et al. The Modern-Era Retrospective Analysis for Research and Applications, Version 2 (MERRA-2). *J. Clim.* **2017**, *30*, 5419–5454. [CrossRef] [PubMed]

102. Rienecker, M.M.; Suarez, M.J.; Todling, R.; Bacmeister, J.; Takacs, L.; Liu, H.-C.; Gu, W.; Sienkiewicz, M.; Koster, R.D.; Gelaro, R.; et al. The GEOS-5 Data Assimilation System—Documentation of Versions 5.0.1, 5.1.0, and 5.2. Technical Report Series on Global Modeling and Data Assimilation, 27, NASA Technical Reports NASA/TM-2008-104606; p. 118. Available online: https://gmao.gsfc.nasa.gov/pubs/docs/Rienecker369.pdf (accessed on 20 January 2021).
103. Molod, A.; Takacs, L.; Suarez, M.; Bacmeister, J. Development of the GEOS-5 atmospheric general circulation model: Evolution from MERRA to MERRA2. *Geosci. Model Dev.* **2015**, *8*, 1339–1356. [CrossRef]
104. Chin, M.; Ginoux, P.; Kinne, S.; Torres, O.; Holben, B.N.; Duncan, B.N.; Martin, R.V.; Logan, J.A.; Higurashi, A.; Nakajima, T. Tropospheric Aerosol Optical Thickness from the GOCART Model and Comparisons with Satellite and Sun Photometer Measurements. *J. Atmos. Sci.* **2002**, *59*, 461–483. [CrossRef]
105. Colarco, P.R.; Da Silva, A.; Chin, M.; Diehl, T. Online simulations of global aerosol distributions in the NASA GEOS-4 model and comparisons to satellite and ground-based aerosol optical depth. *J. Geophys. Res. Atmos.* **2010**, *115*, 14207. [CrossRef]
106. Adler, R.F.; Sapiano, M.R.P.; Huffman, G.J.; Wang, J.-J.; Gu, G.; Bolvin, D.; Chiu, L.; Schneider, U.; Becker, A.; Nelkin, E.; et al. The Global Precipitation Climatology Project (GPCP) Monthly Analysis (New Version 2.3) and a Review of 2017 Global Precipitation. *Atmosphere* **2018**, *9*, 138. [CrossRef]
107. Chedin, A.; Capelle, V.; Scott, N. Detection of IASI dust AOD trends over Sahara: How many years of data required? *Atmos. Res.* **2018**, *212*, 120–129. [CrossRef]
108. Tegen, I.; Miller, R.L. A general circulation model study on the interannual variability of soil dust aerosol. *J. Geophys. Res. Atmos.* **1998**, *103*, 25975–25995. [CrossRef]
109. Wagner, R.; Schepanski, K.; Heinold, B.; Tegen, I. Interannual variability in the Saharan dust source activation—Toward understanding the differences between 2007 and 2008. *J. Geophys. Res. Atmos.* **2016**, *121*, 4538–4562. [CrossRef]
110. Prospero, J.M.; Mayol-Bracero, O.L. Understanding the Transport and Impact of African Dust on the Caribbean Basin. *Bull. Am. Meteorol. Soc.* **2013**, *94*, 1329–1337. [CrossRef]
111. Moulin, C.; Lambert, C.E.; Dulac, F.; Dayan, U. Control of atmospheric export of dust from North Africa by the North Atlantic Oscillation. *Nat. Cell Biol.* **1997**, *387*, 691–694. [CrossRef]
112. Schepanski, K. Transport of Mineral Dust and Its Impact on Climate. *Geoscience* **2018**, *8*, 151. [CrossRef]
113. Hsu, N.C.; Gautam, R.; Sayer, A.M.; Bettenhausen, C.; Li, C.; Jeong, M.J.; Tsay, S.-C.; Holben, B.N. Global and regional trends of aerosol optical depth over land and ocean using SeaWiFS measurements from 1997 to 2010. *Atmos. Chem. Phys.* **2012**, *12*, 8037–8053. [CrossRef]
114. Deflorio, M.J.; Goodwin, I.D.; Cayan, D.R.; Miller, A.J.; Ghan, S.J.; Pierce, D.W.; Russell, L.M.; Singh, B. Interannual modulation of subtropical Atlantic boreal summer dust variability by ENSO. *Clim. Dyn.* **2015**, *46*, 585–599. [CrossRef]
115. Goudie, A.; Middleton, N. Saharan dust storms: Nature and consequences. *Earth Sci. Rev.* **2001**, *56*, 179–204. [CrossRef]
116. Adler, R.F.; Huffman, G.J.; Chang, A.; Ferraro, R.; Xie, P.; Janowiak, J.; Rudolf, B.; Schneider, U.; Curtis, S.; Bolvin, D.; et al. The Version 2 Global Precipitation Climatology Project (GPCP) Monthly Precipitation Analysis (1979-Present). *J. Hydrometeor* **2003**, *4*, 1147–1167. [CrossRef]
117. Gkikas, A.; Houssos, E.E.; Lolis, C.J.; Bartzokas, A.; Mihalopoulos, N.; Hatzianastassiou, N. Atmospheric circulation evolu-tion related to desert-dust episodes over the Mediterranean. *Q. J. R. Meteorol. Soc.* **2015**, *141*, 1634–1645. [CrossRef]
118. Egger, J.; Alpert, P.; Tafferner, A.; Ziv, B. Numerical experiments on the genesis of Sharav cyclones: Idealized simulations. *Tellus A Dyn. Meteorol. Oceanogr.* **1995**, *47*, 162–174. [CrossRef]
119. Hatzianastassiou, N.; Papadimas, C.D.; Lolis, C.J.; Bartzokas, A.; Levizzani, V.; Pnevmatikos, J.D.; Katsoulis, B.D. Spatial and temporal variability of precipitation over the Mediterranean Basin based on 32-year satellite Global Precipitation Climatology Project data. Part-II: Inter-annual variability and trends. *Int. J. Clim.* **2016**, *36*, 4755–4766. [CrossRef]
120. Kaskaoutis, D.; Dumka, U.; Rashki, A.; Psiloglou, B.; Gavriil, A.; Mofidi, A.; Petrinoli, K.; Karagiannis, D.; Kambezidis, H.D. Analysis of intense dust storms over the eastern Mediterranean in March 2018: Impact on radiative forcing and Athens air quality. *Atmos. Environ.* **2019**, *209*, 23–39. [CrossRef]
121. Papadimas, C.D.; Hatzianastassiou, N.; Mihalopoulos, N.; Querol, X.; Vardavas, I. Spatial and temporal variability in aerosol properties over the Mediterranean basin based on 6-year (2000–2006) MODIS data. *J. Geophys. Res. Atmos.* **2008**, *113*. [CrossRef]
122. Hatzianastassiou, N.; Katsoulis, B.; Pnevmatikos, J.; Antakis, V. Spatial and Temporal Variation of Precipitation in Greece and Surrounding Regions Based on Global Precipitation Climatology Project Data. *J. Clim.* **2008**, *21*, 1349–1370. [CrossRef]
123. Hatzianastassiou, N.; Gkikas, A.; Mihalopoulos, N.; Torres, O.; Katsoulis, B.D. Natural versus anthropogenic aerosols in the eastern Mediterranean basin derived from multiyear TOMS and MODIS satellite data. *J. Geophys. Res. Atmos.* **2009**, *114*. [CrossRef]
124. Dey, S.; Di Girolamo, L. A climatology of aerosol optical and microphysical properties over the Indian subcontinent from 9 years (2000–2008) of Multiangle Imaging Spectroradiometer (MISR) data. *J. Geophys. Res. Atmos.* **2010**, *115*, 15204. [CrossRef]
125. Zhao, T.L.; Gong, S.L.; Zhang, X.-Y.; Blanchet, J.-P.; McKendry, I.G.; Zhou, Z.J. A Simulated Climatology of Asian Dust Aerosol and Its Trans-Pacific Transport. Part I: Mean Climate and Validation. *J. Clim.* **2006**, *19*, 88–103. [CrossRef]
126. Tsai, F.; Chen, G.T.-J.; Liu, T.-H.; Lin, W.-D.; Tu, J.-Y. Characterizing the transport pathways of Asian dust. *J. Geophys. Res. Atmos.* **2008**, *113*. [CrossRef]
127. Tian, S.-F.; Inoue, M.; Du, M. Influence of Dust Storm Frequency in Northern China on Fluctuations of Asian Dust Frequency Observed in Japan. *Sola* **2007**, *3*, 121–124. [CrossRef]

128. Kai, Z.; Huiwang, G. The characteristics of Asian-dust storms during 2000–2002: From the source to the sea. *Atmos. Environ.* **2007**, *41*, 9136–9145. [CrossRef]
129. Zhang, B.; Tsunekawa, A.; Tsubo, M. Contributions of sandy lands and stony deserts to long-distance dust emission in China and Mongolia during 2000–2006. *Glob. Planet. Chang.* **2008**, *60*, 487–504. [CrossRef]
130. Vinoj, V.; Rasch, P.J.; Wang, H.; Yoon, J.; Ma, P.-L.; Landu, K.; Singh, B. Short-term modulation of Indian summer monsoon rainfall by West Asian dust. *Nat. Geosci.* **2014**, *7*, 308–313. [CrossRef]
131. Pandey, S.K.; Vinoj, V.; Landu, K.; Babu, S.S. Declining pre-monsoon dust loading over South Asia: Signature of a changing regional climate. *Sci. Rep.* **2017**, *7*, 1–10. [CrossRef]
132. Lakshmi, N.B.; Babu, S.S.; Nair, V.S. Recent Regime Shifts in Mineral Dust Trends over South Asia from Long-Term CALIPSO Observations. *IEEE Trans. Geosci. Remote Sens.* **2019**, *57*, 4485–4489. [CrossRef]
133. Notaro, M.; Alkolibi, F.; Fadda, E.; Bakhrjy, F. Trajectory analysis of Saudi Arabian dust storms. *J. Geophys. Res. Atmos.* **2013**, *118*, 6028–6043. [CrossRef]
134. Klingmüller, K.; Pozzer, A.; Metzger, S.; Stenchikov, G.L.; Lelieveld, J. Aerosol optical depth trend over the Middle East. *Atmos. Chem. Phys.* **2016**, *16*, 5063–5073. [CrossRef]